Biomaterials 320 (2025) 123275

Contents lists available at ScienceDirect

Biomaterials

journal homepage: www.elsevier.com/locate/biomaterials

# Development of an electroconductive Heart-on-a-chip model to investigate cellular and molecular response of human cardiac tissue to gold nanomaterials

Hamid Esmaeili [a], Yining Zhang [b], Kalpana Ravi [a], Keagan Neff [a], Wuqiang Zhu [c], Raymond Q. Migrino [d,e], Jin G. Park [b], Mehdi Nikkhah [a,f,*]

[a] School of Biological and Health Systems Engineering, Arizona State University, Tempe, AZ, 85287, USA
[b] Center for Personalized Diagnostics (CPD), Biodesign Institute, Arizona State University, Tempe, AZ, 85287, USA
[c] Department of Cardiovascular Medicine, Physiology and Biomedical Engineering, Center for Regenerative Medicine, Mayo Clinic, Scottsdale, AZ, 85259, USA
[d] Phoenix Veterans Affairs Health Care System, Phoenix, AZ, 85022, USA
[e] University of Arizona College of Medicine, Phoenix, AZ, 85004, USA
[f] Biodesign Virginia G. Piper Center for Personalized Diagnosis, Arizona State University, Tempe, AZ, 85287, USA

ARTICLE INFO

*Keywords:*
Heart-on-a-chip
hiPSC-CMs
Cardiac tissue
Electrically conductive hydrogels
Gold nanorods (GNRs)
Transcriptomics

ABSTRACT

To date, various strategies have been developed to construct biomimetic and functional *in vitro* cardiac tissue models utilizing human induced pluripotent stem cells (hiPSCs). Among these approaches, microfluidic-based Heart-on-a-chip (HOC) models are promising, as they enable the engineering of miniaturized, physiologically relevant *in vitro* cardiac tissues with precise control over cellular constituents and tissue architecture. Despite significant advancements, previously reported HOC models often lack the electroconductivity features of the native human myocardium. In this study, we developed a 3D electroconductive HOC (referred to as eHOC) model through the co-culture of isogenic hiPSC-derived cardiomyocytes (hiCMs) and cardiac fibroblasts (hiCFs), embedded within an electroconductive hydrogel scaffold in a microfluidic-based chip system. Functional and gene expression analyses demonstrated that, compared to non-conductive HOC, the eHOC model exhibited enhanced contractile functionality, improved calcium transients, and increased expression of structural and calcium handling genes. The eHOC model was further leveraged to investigate the underlying electroconduction-induced pathway(s) associated with cardiac tissue development through single-cell RNA sequencing (scRNA-seq). Notably, scRNA-seq analyses revealed a significant downregulation of a set of cardiac genes, associated with the fetal stage of heart development, as well as upregulation of sarcomere- and conduction-related genes within the eHOC model. Additionally, upregulation of the cardiac muscle contraction and motor protein pathways were observed in the eHOC model, consistent with enhanced contractile functionality of the engineered cardiac tissues. Comparison of scRNA-seq data from the 3D eHOC model with published datasets of adult human hearts demonstrated a similar expression pattern of fetal- and adult-like cardiac genes. Overall, this study provides a unique eHOC model with improved biomimcry and organotypic features, which could be potentially used for drug testing and discovery, as well as disease modeling applications.

## 1. Introduction

Cardiovascular diseases (CVDs) remain the leading cause of death globally [1]. Traditionally, cardiac research has mainly relied on the use of *in vivo* animal models or the use of animal-derived cells, such as neonatal rat ventricular cardiomyocytes (NRVMs), cultured on 2D cell culture assays which lack native human-like physiological relevance. However, due to stark differences in physiology and pharmacokinetics across species, the use of animal models or animal-derived cells in cardiac research could potentially lead to inaccurate interpretations of results, ultimately leading to failure in the clinical translation of the tested therapeutics [2]. The advent of human induced pluripotent stem cells (hiPSCs) [3] has opened enormous opportunities for *in vitro* drug discovery and CVD research, as these cells can be generated from patients

* Corresponding author. School of Biological and Health Systems Engineering, Arizona State University, Tempe, AZ, 85287, USA.
*E-mail address:* Mehdi.Nikkhah@asu.edu (M. Nikkhah).

https://doi.org/10.1016/j.biomaterials.2025.123275
Received 23 October 2024; Received in revised form 16 February 2025; Accepted 17 March 2025
Available online 19 March 2025

with specific disease phenotypes, reducing the reliance on nonhuman animal models and cells [4].

Numerous 3D human cardiac culture systems have been so far developed, ranging from spheroids and organoids [5–9] to engineered heart tissues (EHTs) [10,11] utilizing hiPSCs. These 3D culture platforms show great promise for accurate disease modeling, foundational biological discoveries, as well as drug testing in a physiologically relevant manner [4]. Recently, Organ-on-a-chip systems have also emerged as powerful platform technologies for incorporating specific cellular constituents within an organotypic 3D native-like tissue architecture (e.g., tissue alignment in case of the heart) [12]. Along this line, significant advancements have been made in developing scaffold-free or scaffold-based humanized Heart-on-a-chip (HOC) models [13–18]. For instance, a scaffold-free HOC model was developed by Mathur et al. [15], where monoculture of hiPSC-derived cardiomyocytes (hiCMs) was suspended in the tissue region of a microfluidic chip, resulting in the formation of robust cardiac tissue aligned in a uniaxial manner. In another study, cardiac tissues were formed by incorporating a co-culture of non-isogenic hiCMs and dermal fibroblasts, within a fibrin hydrogel, between two sets of PDMS microposts, resulting in the formation of tissues with adult-like gene expression profile and a remarkably organized ultrastructure [16]. Jayne et al. reported the development of another HOC platform enabling the formation of cardiac microtissues in a controlled microenvironment [17]. In this study, non-isogenic cardiac microtissues, generated by a co-culture of hiCMs and human mesenchymal stem cells (hMSCs), were embedded within a collagen hydrogel matrix for measurement of tissue contraction forces. In line with these studies, we also recently reported the development of an advanced microfluidic HOC model through the incorporation of isogenic hiCMs and hiPSC-derived cardiac fibroblasts (hiCFs) within a cocktail of hydrogel matrix (Collagen-I and Matrigel®) to form a 3D cardiac tissue with native-like tissue organization and cellular constituents [18]. This HOC model was precisely designed and optimized to induce cellular alignment, mimicking the native human myocardium, through the use of elliptical-shaped microposts within the central tissue region of the chip, which promoted cardiac tissue function and maturation-specific gene markers [18], suitable for cardiac disease modeling [19,20].

Despite the significance and notable findings of the previous works, including ours, the 3D cardiac tissue microenvironments formed within the reported HOC models often lacked electroconductivity cues, resembling the native human myocardium [21]. In prior cardiac tissue engineering studies, electrically active hydrogel scaffolds have been proposed by embedding electroconductive components, such as carbon-based nanomaterials [22–26], electroconductive polymers [27,28], and gold nanomaterials [29–34] to promote tissue function and maturation. These synthesized conductive scaffolds specifically improved the contractile function of NRVMs as well as hiCMs by enhancing cellular crosstalk and gap junction proteins, thereby facilitating electrical signal propagation across the tissue [35]. In line with this, recently, a HOC model was developed by integrating electroconductive aligned carbon nanotubes into GelMA hydrogel within a PDMS-based microfluidic chip [36]. Specifically, NRVMs were monocultured atop the electroconductive substrate inside the HOC tissue channel, resulting in enhanced cellular alignment and rhythmic beating of the cardiac tissue. However, the development of a humanized 3D electrically conductive HOC model, comprising of isogenic hiPSC-derived cardiac tissues with native-like cellular composition and anisotropic architecture, is still missing in previous studies. Additionally, while bulk RNAseq has been utilized to assess the role of tissue environment, such as electrical conductivity of the hydrogel matrix on phenotype of hiPSC-derived cardiac cells [37], there is still a knowledge gap regarding the role of electroconductive nanomaterials, utilizing single-cell RNA sequencing (scRNA-seq), in further exploring the molecular mechanisms that govern enhanced functionalities of the engineered cardiac tissues.

To address these knowledge gaps, in this work, we developed a 3D electroconductive HOC model (referred to as eHOC), which incorporates a highly organized tissue architecture derived from the isogenic co-culture of hiCMs and hiCFs. We further mechanistically assessed the role of electrical conductivity features of the 3D tissue environment, induced by the presence of gold nanorods (GNRs), on the functionalities and phenotype of the cardiac tissue. Specifically, we utilized GNRs to generate electrically active hydrogel scaffolds within the HOC microfluidic model, complementing and advancing our previous work as well as that of others [29,38,39], due to their biocompatibility, surface functionalization capabilities, and stable electroconductivity [40,41]. The nanoengineered hydrogel scaffolds, were synthesized by incorporating various concentrations of GNRs (~42 nm in length, ~11 nm in diameter, and with an aspect ratio of ~4) within a cocktail of Collagen-I and Matrigel® (Col-I:Matrigel®) hydrogel matrix. Upon formation of the model, we performed extensive biological characterization including immunofluorescence (IF) staining of cardiac-specific markers, beating and calcium transient ($Ca^{2+}$) analyses, as well as gene expression to assess the fate and functionality of the cultured hiCMs within the eHOC tissue environment. Notably, scRNA-seq was further performed to unveil the differentially expressed genes (DEGs) between the control group (non-conductive HOC) and the eHOC model, along with the underlying pathways that could potentially contribute to the enhanced functionality of the hiCMs co-cultured with hiCFs. The electroconductive cardiac tissue formed within the eHOC model demonstrated enhanced functionalities of hiCMs displayed by improved contractility and $Ca^{2+}$ handling properties. Furthermore, gene expression and scRNA-seq analyses showed that the improved functional characteristics of the tissue correlated with the increased expression of genes involved in calcium handling, conduction, and sarcomere-related processes, such as *GJA1, TNNI3, and ACTN2*. To the best of our knowledge, this study is the first to utilize scRNA-seq to mechanistically assess the role of electrically conductive nanomaterials on functionalities of isogenic cardiac tissues (hiCMs and hiCFs) within an eHOC model. The proposed model system could be a valuable tool for representation of a physiologically relevant and *in vivo* like human myocardial tissue microenvironment for enhanced drug testing and disease modeling applications.

## 2. Materials and methods

### 2.1. Materials

The list of the used materials is summarized in Supplementary Table S1.

### 2.2. Methods

#### 2.2.1. Fabrication of the HOC model

The HOC model was created using the photo and soft lithography technique, as previously detailed [18,42]. Briefly, the master silicon wafer was fabricated using the photo lithographic technique. The device design consists of a central tissue region consisting of staggered elliptical micropost spaced evenly at 150 μm. To allow for nutrient and oxygen diffusion, the tissue region was surrounded by two flanking media channels bordered by trapezoidal microposts spaced at 100 μm, which essentially separates the tissue region from the media channel. The overall length and height of the device are 200 μm and 100 μm, respectively. Upon fabricating the master mold, the microfluidic devices are formed using the soft lithographic technique. Specifically, the master mold are coated with methyltrichlorosilane (MTCS) to increase the hydrophilicity of the silicon wafer and reduce attraction between PDMS and SU8 features. A mixture of PDMS base and crosslinker, in a 10:1 ratio, was poured onto the master silicon wafer, followed by a 20 min degassing process to eliminate the trapped air. Subsequently, the mixture was cured at 80 °C for 2 h. The PDMS mold was then separated from the master mold, and 1 mm and 1.5 mm holes were created for the media channels and tissue channels using biopsy punches. The

individual PDMS devices were bonded to 18 × 18 mm coverslips using oxygen plasma (PDC-32G, Harrick Plasma), and this was followed by overnight baking at 80 °C to secure the attachment of PDMS and glass substrates. Prior to the injection of cardiac cells and media, the devices underwent sterilization through both a liquid and a gravity cycle in an autoclave.

#### 2.2.2. Differentiation of human iPSC-derived cardiomyocyte (hiCM)

hiPSCs (IMR90-4, WiCell) were cultured in Matrigel®-coated 6-well plates using mTeSR Plus medium. Passaging was performed when the cells reached approximately 80 % confluency. The utilized medium was aspirated, and the cells were gently washed with PBS. Subsequently, dissociation was carried out with 0.5 mM EDTA (1 mL per well) for about 6 min. Following the removal of EDTA, 1 mL of mTeSR Plus medium was used to mechanically detach and plate the cells onto a separate Matrigel®-coated well.

The GiWi differentiation protocol, with slight adjustments, was employed to induce the differentiation of hiPSCs into hiPSC-CMs (hiCMs) [43]. Initially, hiPSCs were seeded on Matrigel®-coated 6-well plates with a specific seeding density (~0.1–0.15 M cells per well). When cell confluency reached approximately 85–90 %, the mTeSR Plus medium was gently aspirated, and the cells were washed once with 1 mL of PBS per well. Subsequently, the PBS was removed, and RPMI/B27 without insulin (RPMI/B27 (-Ins)) medium (3 mL per well) supplemented with 6 μM GSK3-β inhibitor CHIR99021 (CHIR) was added and maintained for 24 h. After 24 h (day 1), 2 mL of RPMI/B27 (-Ins) was added to each well for an additional 24 h (until day 2). On day 2, another 1 mL of RPMI/B27 (-Ins) was added to each well and maintained for 24 h (until day 3). On day 3 of differentiation, the used medium was discarded, and the cells were gently washed with 1 mL of PBS per well. Then, 3 mL of RPMI/B27 (-Ins) supplemented with 3 μM Wnt inhibitor IWR1 was added to each well and maintained for another 48 h. The medium was changed to RPMI/B27 (-Ins) (3 mL per well) on days 5 and 7 of differentiation. On day 9, the old medium was removed, and RPMI/B27 (with insulin) (3 mL per well) was added and replenished every other day until day 15. The spontaneous beating of hiCMs was typically observed on days 9–11 of differentiation. Purification of the hiCMs was achieved through a glucose-depleted culture medium containing lactate [44]. On day 15 post-differentiation, the medium was switched to the glucose-depleted RPMI/B27 (with insulin and 5 mM sodium $_{L}$-lactate) medium (4 mL), and this medium was maintained until day 19. On day 19, the medium was changed back to RPMI/B27 (with insulin) medium (3 mL). Before using the differentiated hiCMs to form cardiac tissues, hiCMs were maintained in a 2 mL serum- and supplement-free medium for an additional 24 h to synchronize their cell cycle. 25–28 days old hiCMs were utilized throughout the experiments.

#### 2.2.3. Differentiation of isogenic human iPSC-derived cardiac fibroblast (hiCFs)

hiCFs were generated through an established protocol with slight modification [45]. Briefly, hiPSCs (IMR90-4) were dissociated using a 0.5 mM EDTA solution in PBS (1 mL per well) at room temperature for approximately 6 min. The dissociated cells were then plated on Matrigel®-coated 6-well plates at the density of 0.1-0.15 × $10^6$ cells per well in mTeSR Plus medium. The cells were maintained in mTeSR Plus medium for 3–4 days, with daily medium changes, until reaching 80–90 % confluence. On day 0, the medium was replaced with 4 mL of insulin-free RPMI/B27 containing 7 μM CHIR99021. After 24h (day 1), the medium was switched to 5 mL of insulin-free RPMI/B27 and maintained for an additional 24 h (day 2). Then, the media was removed, and 2.5 mL of hiCF differentiation medium (hCFBM) containing 70 ng/uL bFGF was added per well for another 48 h (day 4). Following day 4, cells were provided with 2.5 mL hCFBM supplemented with 70 ng/uL bFGF every other day until day 20 when cells were passaged and cryopreserved for future use. Beyond day 20, the differentiated hiCFs were either cryopreserved or passaged and maintained in FGM3 media.

#### 2.2.4. Formation of the electroconductive HOC (eHOC) model

GNRs were first synthesized and characterized following the procedures detailed in our previously published papers [29]. To nanoengineer the electrically active scaffolds, concentrated GNRs were incorporated into hydrogels composed of Col-I:Matrigel® (80:20) with final concentrations of 0.0 mg/mL, 0.2 mg/mL, and 0.5 mg/mL, and 1.0 mg/mL. The hydrogel prepolymer solutions were thoroughly mixed and maintained on ice until their final use in the HOC devices. Scanning electron microscopy (SEM) imaging (Zeiss Auriga) was employed to assess the ultrastructure and porosity of the lyophilized hydrogel scaffolds. The hydrogel scaffolds underwent freezing in liquid nitrogen, lyophilization, and carbon coating. They were then imaged at 5 kV. For assessing the distribution of the GNRs within the hydrogel scaffold, 80 μl of the hydrogel prepolymer were pipetted into 1.7 mL microcentrifuge and crosslinked for 25 min at 37 °C. Then hydrogel scaffolds were frozen in liquid nitrogen, lyophilized, and gold coated. They were then imaged at 5 kV.

For evaluating the electrical conductivity properties, a two-probe measurement method using an electrochemical impedance spectroscopy (EIS) potentiostat was employed to assess the impedance of the nanoengineered hydrogel scaffolds. Specifically, hydrogel scaffolds (HOC-0.0, eHOC-0.2, eHOC-0.5, and eHOC-1.0) were prepared as mentioned above and loaded between two glass slides coated with indium tin oxide. At a 10-mV applied voltage, the impedance of each hydrogel scaffold was examined from 1.0 Hz to 100 kHz. The mechanical characterization of hydrogels composed of Col-I: Matrigel® (80:20) with final GNR concentrations of 0.0 mg/mL, 0.2 mg/mL, 0.5 mg/mL, and 1.0 mg/mL was measured by analyzing their compressive modulus. Specifically, 70 μl of the prepolymer solutions were pipetted into cylindrical molds and crosslinked for 25 min at 37 °C. Then, the compressive modulus was measured at a rate of 13 μm/s on an Instron (Instron 5943, 50 N load cell). The modulus was calculated by analyzing the slope of the linear region corresponding to 1–5 % strain in the stress vs. strain curve.

Differentiated hiCMs and hiCFs from hiPSCs were then encapsulated within the nanoengineered hydrogel scaffolds, achieving a final seeding density of 35 M/mL, with a hiCMs to hiCFs ratio of 4:1. The ratio of hiCMs: hiCFs were experimentally determined, based on our previous study [18]. The hydrogel-cell mixture was gently pipetted up and down to ensure the homogenous distribution of cells within the scaffolds. To form the cardiac tissues, approximately 3 μL of each nanoengineered hydrogel-cell combination (containing approximately 100K cells/device) was injected into individual devices resulting in **HOC-0.0**, **eHOC-0.2**, **eHOC-0.5**, and **eHOC-1.0**. The hydrogel cell mixture was carefully injected into the tissue region, ensuring that the tissue region was completely covered. After injection, devices were cross-linked for 18 min at 37 °C with an intermediate flipping step at 9 min. The established tissues were cultured for 14 days in RPMI + B27 plus insulin, and the media was exchanged every day. The tissue filled the entire culture region within the HOC surrounded by two media channels. The size of the established tissue was about 200 μm in length and 100 μm in height.

#### 2.2.5. Cell viability assay

A Live/Dead kit was employed following the manufacturer's instructions. The combination of hiCMs and hiCFs in a 4:1 ratio, encapsulated within nanoengineered hydrogel scaffolds, was cultured for 2 days in the HOC model. Subsequently, the samples were then gently washed once with 1X PBS. The tissues were immersed in a solution containing 4 μM EthD-1 and 2 μM calcein-AM for 20 min at room temperature. Following this incubation, the samples were washed with 1X PBS before imaging.

*2.2.6. Immunofluorescence (IF) staining*

On day 14 of the culture, the spent medium was gently aspirated from the medium channels, and the cardiac tissues were washed once with 1X PBS before fixation in 4 % paraformaldehyde for 15 min at 37 °C. Following fixation, the samples underwent three washes with PBS-glycine, each lasting 10 min at room temperature. Subsequently, cell permeabilization was achieved with Triton-X-100 (1 %) for 30 min at room temperature. The tissues were then blocked using a solution of goat serum in PBS-tween-20 (10 %) for 1 h at room temperature. Next, primary antibodies were diluted in the same blocking solution and injected into the medium channels followed by overnight incubation at 4 °C. The primary antibodies used in this study included Alexa Fluor 488 Phalloidin (1:1000), mouse monoclonal anti-sarcomeric alpha-actinin (1:100), and rabbit polyclonal anti-connexin 43 (1:100). After the overnight incubation, the tissues were washed at room temperature five times with PBS-tween-20, each lasting 10 min. Secondary antibodies were then diluted in 4',6-diamidino-1-phenylindole (DAPI) (1:1000) and centrifuged at 18.8k *g* for 10 min to remove aggregates and impurities. The tissues were stained with secondary antibodies for 1 h at room temperature. In this study, Alexa Fluor 488 goat anti-rabbit (1:400) and Alexa Fluor 647 goat anti-mouse (1:400) were used as secondary antibodies. Imaging was conducted at 63X and 100X magnifications using confocal microscopy for the samples stained with SAA/Cx43. Other stained samples were analyzed using a Zeiss microscope (Observer Z1) equipped with Apotome2 at 10X and 20X objectives. Finally, the Fiji software [46] was used to process the z-stack images.

*2.2.7. Analyses of contractility and beating behavior of cardiac tissues*

The analysis of cardiac tissue beating behavior followed the methodology described in our recent publications [18,20]. Briefly, cardiac tissue samples were positioned on the stage of a Zeiss microscope, and phase-contrast images were captured on day 14 of the culture using a 10X objective. Time-lapse images (25 fps) were recorded (10X) for 20s on day 14 to observe the spontaneous contractions of the cardiac tissues. Information regarding beating patterns, beats per minute (BPM), and inter-beat interval variability (IIV) was extracted using a custom-written MATLAB code. To assess IIV, the contraction peaks and their corresponding times were extracted from the recorded videos using MATLAB code. The standard deviation of the contraction peak times was then calculated and reported as IIV, serving as a measure of beating regularity. Additionally, motion data, including contraction amplitude and relaxation time of the spontaneously beating cardiac tissues, was also extracted from the recorded videos (35 frames per second (fps)) using the open-source macro MUSCLEMOTION for Image J [47].

*2.2.8. Electrophysiological analysis of the cardiac tissues*

For calcium transient imaging, 14-day-old tissues underwent incubation with the calcium indicator (Fluo-4-AM in Pluronic) at 37 °C for 45 min, followed by rinsing in Tyrode's solution at 37 °C for 25 min. Videos were recorded with a 60 ms exposure time at 16.3 fps using a Zeiss fluorescence microscope at 488 nm wavelength. To generate calcium spike traces, the recorded videos were analyzed using the Fiji software [46], and the background fluorescence intensity was subtracted from the fluorescence intensity of calcium spikes (F), resulting in background-corrected changes in fluorescence values for each frame (ΔF). The ΔF values were then divided by the minimum fluorescence intensity of calcium spikes from the same spot to obtain ΔF/F0 values and plotted against time [48].

*2.2.9. Gene expression*

Reverse-transcription quantitative polymerase chain reaction (RT-qPCR) was employed to assess the relative expression levels of a set of cardiac-specific genes. After a two-week culture period, the cardiac tissues developed on the hydrogel scaffolds underwent incubation with prewarmed Collagenase-I (4 mg/mL) at 37 °C for 45 min. The digested cells were then collected in Eppendorf tubes and centrifuged for 3 min at 300 *g*. After discarding the supernatant, the pellets were lysed using a lysis buffer (250 μL). Subsequently, RNA extraction from the cell lysates was carried out using the Quick-RNA MicroPrep Kit (Zymo Research; Cat# R1050) in accordance with the manufacturer's protocol. The purity and concentration of the extracted RNA were analyzed through 260/280 nm absorbance using the Nanodrop One instrument (Thermo Scientific). Following this, iScript Reverse Transcriptase Supermix (Bio-Rad) was used to synthesize cDNA from the extracted RNA. The synthesized cDNA was then analyzed through qPCR using the iTaq Universal SYBR Green Supermix (Bio-Rad). Melt curve analysis and verification of qPCR product size were employed to validate the designated set of primers as shown in Table S2. The qTower 2.0 was then utilized for qPCR analysis and the delta-delta Ct method ($2^{-\Delta\Delta Ct}$) with 18S as the housekeeping gene was utilized to quantify the relative gene expression fold change. A suspension of hiCMs and hiCFs at day 0 (D0) prior to culture on hydrogel scaffolds was utilized for normalizing the relative gene expression levels. The row Z-score for each gene was calculated based on the fold changes of each experimental group and presented in an expression heatmap using GraphPad Prism software.

*2.2.10. Single-cell RNA sequencing (scRNA-seq)*

On day 14 of culture, cardiac tissues formed within **HOC-0.0** and **eHOC-0.5** were dissociated into single cells using Collagenase-I at 37 °C for 45 min. The dissociated cells were passed through 70-μm filters to generate a homogenous single-cell suspension. Once single-cell suspensions were achieved, cardiac cells were fixed following the *PARSE Biosciences Evercode™ Fixation* manual. scRNA-seq libraries were prepared using the *PARSE Biosciences kit (WT Mini V2)* following the manufacturer's protocol. In brief, 18,000 cells from three groups (two biological replicates for each condition resulting in 6 samples) were split into 12 wells for the first round of sample barcoding, and the final pooled cells were divided into two equal libraries for sequencing. Libraries were subsequently sequenced on a NovaSEQ6000. Following this, the raw sequencing data obtained from the experiments were preprocessed using the pipeline supplied by Parse Biosciences (v1.1.1). The reference genome and annotation files used in the data processing are GRCh38 and Ensemble 110. The function `ReadParseBio` in Seurat (v4.4.0) was used to read the count matrix in the output of Parse Biosciences pipeline. As of the count matrix, the genes that are detected in at least 12 cells were kept. Also, pseudogenes were excluded from the matrix. The following criteria were used for filtering out cells: 1) total counts per cell <200,000; 2) number of detected genes per cell <15,000. For the remaining 5789 cells after filtering, the cell cycle scores were calculated using the function 'CellCycleScoring'. The filtered count matrix was normalized using the function 'SCTransform' to mitigate technical variability across cells. During normalization, mitochondrial mapping percentage and cell cycle scores were considered as confounding sources of variation and removed. All remaining genes in the normalized matrix were used to perform a Principal Component Analysis (PCA). At a resolution of 0.7, cell clustering analysis by the Louvain algorithm was performed using the first 50 principal components, resulting in a total of 12 clusters. Uniform Manifold Approximation and Projection (UMAP) was employed to visualize the high-dimensional data in two dimensions. The cell type of each cluster was determined based on the average expression levels of marker genes within each cluster.

To identify differentially expressed genes (DEGs) in cardiomyocytes across different treatment groups, the average expression levels for cardiomyocytes in each sample were calculated using the AverageExpression function in Seurat. An ANOVA was then performed to compare the expression levels across the three treatment groups. Genes with a p-value less than 0.05 were considered significantly differentially expressed in at least one treatment group. These genes were used to generate the heatmap, where the average expression levels were standardized using Z-score transformation. For group-wise analysis, the two replicates for each treatment group were combined, and differential expression analysis was performed on cardiomyocytes using the

FindMarkers function in Seurat. A volcano plot was generated to visualize the results, with genes having an adjusted p-value less than 1e-10 considered significantly differentially expressed. Mitochondrial genes were excluded from the analysis.

To compare the expression levels of cardiomyocytes between 3D and 2D cultures, the FindMarkers function was used to perform differential expression analysis for each cardiomyocyte cluster. The results were visualized using a volcano plot. The FindAllMarkers function was used to identify the top upregulated genes in each cluster. For the top two upregulated genes in each cluster, the VlnPlot function was used to generate violin plots to visualize their expression differences across clusters.

The raw counts of cardiomyocytes in the scRNA-seq data were aggregated based on conditions. The expression levels of genes related to structural, conduction, and calcium handling were CPM-normalized and then log-transformed. The transformed data was visualized using a heatmap.

For pathway enrichment analysis, identified DEGs were filtered based on an adjusted p-value cutoff of less than 0.01 to generate upregulated and downregulated gene lists. Mitochondrial and ribosomal protein genes were excluded from these lists. Pathway enrichment analysis was performed using the enrichKEGG function from the clusterProfiler package. Pathways with a p-value less than 0.01 were visualized using a bar plot. From the enriched pathways, selected pathways of interest were further visualized using the cnetplot function to create gene-concept networks.

For comparison with human *in vivo* samples, Raw FASTQ data were downloaded from public repository NCBI GEO/SRA, with Fetal_120 (SRR643778), Fetal_91 (SRR643779), and four LV samples (SRR577587, SRR577588, SRR577589, SRR577590). These data were aligned to the reference genome using STAR, and gene counts were obtained for each sample. For the LV samples, gene counts from the four runs were averaged and rounded to produce a composite LV_avg dataset. An expression matrix was constructed using Fetal_120, Fetal_91, and LV_avg. Lowly expressed genes and mitochondrial genes were filtered out, and the matrix was normalized using the TMM method. Pairwise differential expression analysis between the three samples was conducted using the exactTest function in edgeR, with the biological coefficient of variation (bcv) set to 0.4. Genes with an FDR $<0.05$ were considered differentially expressed. The union of differentially expressed genes (DEGs) from all pairwise comparisons was taken as the DEG list for bulk data, which was then intersected with the DEG list from 3D model to obtain the final DEG list. For single-cell RNA sequencing data from 3D model, only cardiomyocytes were kept. Raw counts were extracted for each cell and normalized using counts per million (CPM) normalization. For comparison with human *in vivo* samples, Raw FASTQ data were downloaded from public repository NCBI GEO/SRA, with Fetal_120 (SRR643778), Fetal_91 (SRR643779), and four LV samples (SRR577587, SRR577588, SRR577589, SRR577590). These data were aligned to the reference genome using STAR, and gene counts were obtained for each sample. For the LV samples, gene counts from the four runs were averaged and rounded to produce a composite LV-avg dataset. An expression matrix was constructed using 91-day fetus heart sample, 120-day fetus heart sample, and adult LV sample. Lowly expressed genes and mitochondrial genes were filtered out, and the matrix was normalized using the TMM method. Differential expression analysis between fetus heart samples and adult LV sample was conducted using the exactTest function in edgeR, with the biological coefficient of variation (bcv) set to 0.4. Genes with an FDR $<0.01$ were considered differentially expressed. The DEGs from bulk data were then intersected with the DEGs from the 3D model **(Supplementary table 3)** to obtain the final DEG list. For single-cell RNA sequencing data from the 3D model, only cardiomyocytes were kept. Raw counts were extracted for each cell and normalized using Counts per million (CPM) normalization. The mean expression for each treatment group was calculated to generate the single-cell expression matrix. The CPM normalized bulk expression matrix and single-cell expression matrix were then transformed to log2 scale and followed by Z-score standardization separately. Heatmaps were generated to visualize the results.

#### 2.2.11. Statistical analysis

Unless otherwise stated, all quantitative data were presented as means ± standard deviation (SD) with three biological replicates. One-way ANOVA with Tukey's post-hoc analysis was performed when the data sets had more than two experimental groups. Student's *t-test* was used for the analysis of data sets with two experimental groups. GraphPad Prism software version 6 was used to evaluate the statistical analyses, with p-values $<0.05$ considered significant. For differential expression and pathway analysis for scRNA-seq data, p-values were adjusted for multiple testing by the Benjamini-Hochberg's False Discovery Rate (FDR) method.

## 3. Results

### 3.1. Development of electroconductive heart-on-a-chip (eHOC) model

The development of biomimetic HOC models utilizing human induced pluripotent stem cells (hiPSCs) has been a promising approach for cardiac research [13–18]. Despite significant advancements, electroconductivity features, which are an inherent characteristic of native human myocardial tissue, are often neglected when developing the biomimetic microenvironment within the HOC models. To address this, we aimed to incorporate electrically active (i.e., conductive) hydrogel scaffolding biomaterial within an HOC model to replicate the electroconductive microenvironment of the native heart tissues. The schematic overview of the development of the electroconductive HOC (referred to as eHOC) model is depicted in Fig. 1A. Similar to our recently published studies [18–20], elliptical-shaped microposts were integrated into the tissue channel of the HOC model for anisotropic alignment of cardiac tissues, mimicking the natural alignment found in native human myocardium. To form the tissue within the HOC model, we primarily nanoengineered electrically active hydrogel scaffolds, utilizing electroconductive gold nanorods (GNRs) embedded within a cocktail of Col-I: Matrigel® hydrogel scaffolds for cellular encapsulation and injection into the tissue region of the microfluidic HOC model (Fig. 1A). The GNRs, synthesized based on established protocols of ours and others [29, 49], and characterized using UV–Vis spectra analysis, revealed the presence of transverse surface plasmon resonance (TSPR) and longitudinal surface plasmon resonance (LSPR) around 510 nm and 790 nm, respectively (Fig. S1A). The TSPR and LSPR correspond to the formation of rod-shaped gold nanoparticles associated with the short and long axis, respectively. Further analysis of GNRs using transmission electron microscopy (TEM) imaging confirmed the synthesis of a pure population of these nanoparticles (Fig. S1B). Consistent with our recent studies [29, 39], GNRs with an aspect ratio of approximately 4.0 (length/diameter) and approximate dimensions of 43 nm in length and 12 nm in diameter were used in this study.

The concentrations of GNRs in the hydrogel solutions were measured using a standard curve, as described in our recent publication [39]. Various studies, including ours, have explored different concentrations of GNRs ranging from 0.1 to 1.0 mg/mL within hydrogel scaffolds to generate an electroconductive microenvironment for cardiac tissue engineering [29,50,51]. To identify the optimal concentration of GNRs within the 3D HOC model, we developed four experimental groups by incorporating 0.0 mg/mL (**HOC**, as Control), 0.2 mg/mL (**eHOC-0.2**), 0.5 mg/mL (**eHOC-0.5**), and 1.0 mg/mL (**eHOC-1.0**) of GNRs into the Col-I: Matrigel® hydrogel matrix (Fig. S1C). To form the cardiac tissues, a co-culture of isogenic hiCMs and hiCFs with a 4:1 ratio and a final seeding density of 35 M/mL was encapsulated within the nanoengineered electrically conductive hydrogel prepolymer solutions, within the designated experimental condition, followed by gentle pipetting to ensure the homogenous distribution of cardiac cells within

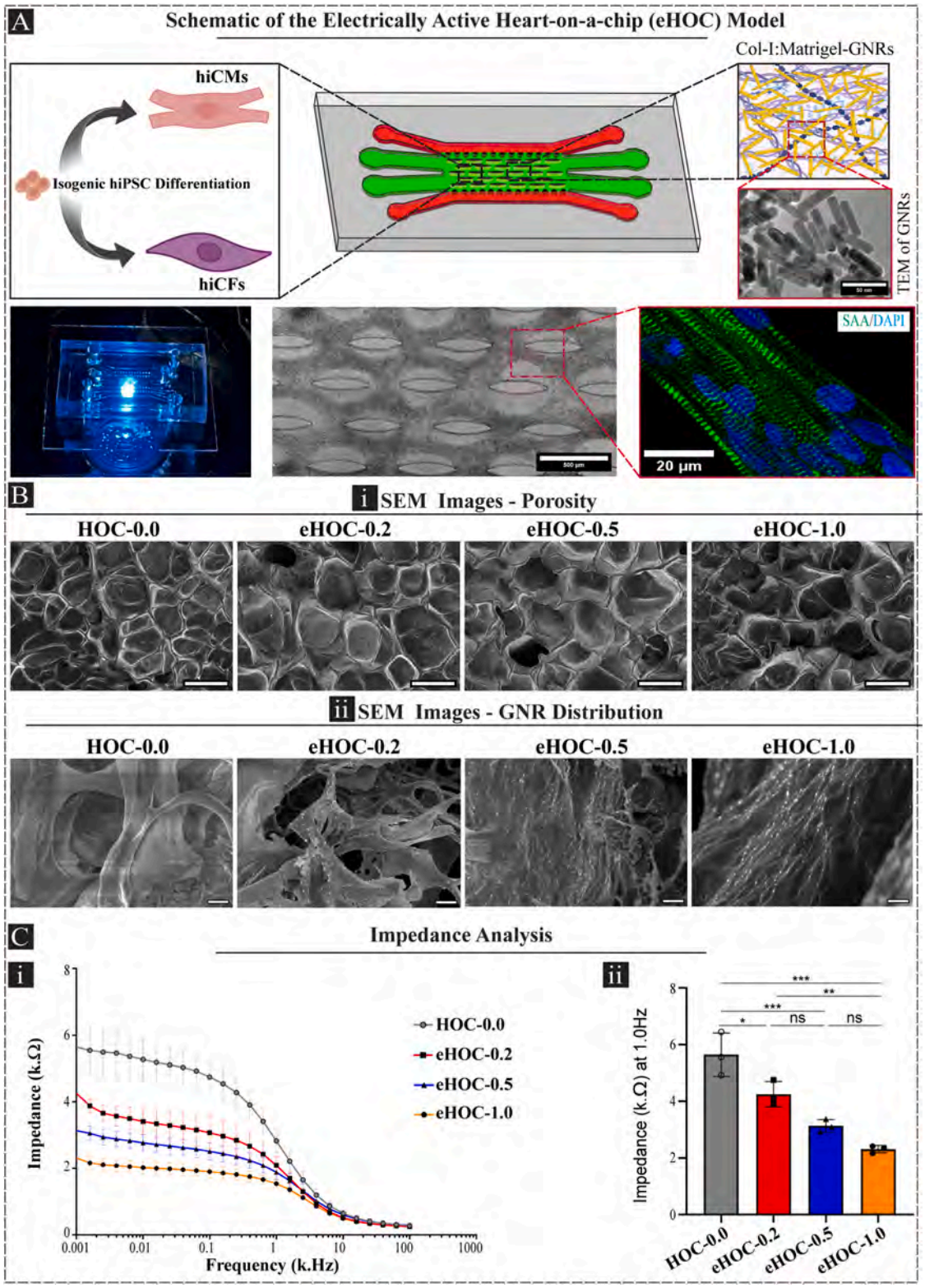


**Fig. 1. Development of electroconductive Heart-on-a-chip (eHOC) model. A**) A schematic illustration of the components of the eHOC model. Isogenic hiCMs and hiCFs encapsulated within nanoengineered electrically active hydrogel scaffolds. Representative image of the actual HOC placed on a microscope stage (bottom left), bright field image of the tissue within the eHOC model captured on day 14 (bottom middle), and IF image of the 14 days cardiac tissue stained for SAA and DAPI showing the alignment of the sarcomere structures (bottom right). **B**) Characterization of the nanoengineered hydrogel scaffolds used in HOC-0.0, eHOC-0.2, eHOC-0.5, and eHOC-1.0, using SEM imaging (cross-sectional view). No apparent differences were observed in the morphology of hydrogel scaffolds with various concentrations of GNRs (**i**), and closer examination of the scaffold demonstrated distribution of GNRs in the matrix across various experimental conditions **(ii)**. The scale bar is 50 μm (top panel) and scale bar 2 μm (bottom panel). **C**) Conductivity analysis of the nanoengineered hydrogel scaffolds measured by two-point probe analyses. Bode diagram of the nanoengineered hydrogel scaffolds at various frequencies (**i**) and impedance of these hydrogel scaffolds at 1.0 Hz measured by EIS Potentiostat (**ii**). Data were expressed as mean ± standard deviation. $*p < 0.05$, $**p < 0.01$, $***p < 0.001$, and ns (not significant) (one-way ANOVA with a Tukey's *post-hoc* test, n = 3).

the scaffolds. Then, approximately 3 μL of each cell-hydrogel mixture (containing approximately 100K cells/device) was injected into the cardiac tissue channel of the HOC model, followed by incubation at 37 °C for the gelation of the hydrogel scaffolds. Similar to our previous studies on the development of cardiac tissues in the 3D HOC model [18], the tissues in this study were also cultured for 14 days before conducting downstream biological assessments. A representative photo of the microfluidic HOC along with the formed cardiac tissue within the chip, exhibiting a highly organized structure, has been shown in Fig. 1A.

Despite using various concentrations of GNRs embedded within the hydrogel scaffolds, no apparent differences were observed in the structure of the nanoengineered hydrogel scaffolds revealed by SEM (Fig. 1B). SEM images revealed a porous structure in the hydrogel mixture (Fig. 1B**(i)**), while higher magnification analysis showed the distribution of the GNRs within the matrix (Fig. 1B**(ii)).** Specifically, we noted differences in GNR distribution within the hydrogel matrix, with more GNR present throughout the scaffold in the case of eHOC-1.0 (highest concentration of GNRs) and the absence of GNR in HOC-0.0 (Control) as expected. On the other hand, eHOC-0.5 and eHOC-0.2 exhibited lower GNRs as compared to eHOC-1.0, confirming the differences across experimental conditions. No significant differences in the GNRs distribution were observed between eHOC-0.5 and eHOC-0.2 groups **(**Fig. 1B**(ii))**. Additionally, we also measured the mechanical property of the nanoengineered hydrogel scaffolds through compressive testing, to ensure the physiological stiffness of the synthesized material before encapsulation of the cells [52]. Quantification of the compressive modulus revealed the stiffness across various groups remained the same irrespective of the addition of the GNRs (Fig. S1D). Impedance analysis was then conducted to assess the effect of GNRs on the conductivity of the nanoengineered hydrogel scaffolds. Previous studies have reported that increasing GNR content within hydrogel scaffolds resulted in enhanced conductivity, as indicated by reduced impedance of the tested scaffolds [29]. The Bode diagram extracted from the two-point measurement setup illustrated that the impedance of hydrogel matrices formed within eHOC-0.2, eHOC-0.5, and eHOC-1.0 was lower than that of eHOC-0.0 across the entire frequency range (Fig. 1C**(i)**). Additionally, the impedance of the hydrogel matrices was quantitatively measured at 1.0 Hz. It was observed that the impedance of the GNR-embedded hydrogel matrices, within the eHOC models, was significantly reduced — approximately 0.6-fold for eHOC-0.2 and 2-fold for eHOC-0.5 and eHOC-1.0 conditions as compared to control HOC (0.0 GNRs) (Fig. 1C **(ii)**). Interestingly, while there was a reduction in the impedance of eHOC-1.0 compared to eHOC-0.5, the two-fold increase in GNR concentration did not lead to a significant increase in the electrical conductivity of this group. In summary, eHOC models with varying levels of electroconductivity were developed by incorporating various concentrations of GNRs within the hydrogel scaffolds.

### 3.2. *Viability and cytoskeleton analysis of the cardiac tissues formed in eHOC model*

For biological studies, initially, a live and dead assay was performed to evaluate the cytocompatibility of the HOC models on day 3 of culture. It was revealed that eHOC models had no negative impact on the viability of the cardiac cells, with viability reaching approximately 95 %, similar to the control group (Fig. 2A and Fig. S2). Since no significant differences in cytotoxicity were observed among the HOC models, we continued our biological analysis with all the designated experimental groups (**HOC**, **eHOC-0.2**, **eHOC-0.5**, and **eHOC-1.0**).

Next, we evaluated the morphology of the cardiac tissues within the 3D eHOC models. Phase-contrast images from day 3 of culture demonstrated that cardiac cells were homogenously distributed within the cardiac tissue channels of the HOC models, with no apparent difference among the conditions (Fig. S3A). Phase-contrast images from day 14 of culture (Fig. S3B) revealed that cardiac cells formed tissue bundles between the microposts of the HOCs, resulting in narrower tissue morphology, possibly due to contraction of the encapsulated hiCMs, as observed in our previous studies [18–20]. To further evaluate the cytoskeleton and ultrastructure of cardiac tissues within the HOC model, the tissues were stained against F-actin fibers. While no apparent differences were observed among the cardiac tissues formed within the eHOCs with lower concentrations of GNRs (i.e., eHOC-0.2 and eHOC-0.5), in contrast cardiac cells within the eHOC-1.0 did not form a robust tissue structure bundle (Fig. 2B and Figs. S4–S5A). In our recent publication, the integrated microposts within the HOC model were found to enhance tissue alignment and the directionality of cardiac tissues over time [18]. Similarly, in this work, our quantitative analysis of cardiac tissue fibers showed that the presence of GNRs within the tissue microenvironment did not significantly impact fiber directionality, where majority of tissue fibers were oriented around −20 and −30° due to the presence of the microposts within the tissue region of the chip. (Fig. 2C). However, with higher concentrations of GNRs, namely eHOC-1.0, there was a significant reduction in coherency values, an index of the directionality of the tissue (Fig. 2D), indicating less aligned cardiac tissues in this culture condition. Based on these assessments, we speculate that less directional fiber formation in eHOC-1.0 within the model system was due to the lack of efficient cell-cell and cell-matrix interactions in the presence of high concentrations of GNRs.

To evaluate whether the 3D eHOC models influenced cardiac-specific markers involved in the contractile apparatus machinery of hiCMs, the tissues were fixed at day 14 and stained for sarcomeric alpha-actinin (SAA) and connexin 43 (Cx43). The sarcomere structure of hiCMs was found to be elongated along the axis of the tissue, likely due to the influence of the passive tension between the microposts exerted by the contraction-relaxation of the cells. While hiCMs in HOC-0.0, eHOC-0.2, and eHOC-0.5 groups developed striated and well-established sarcomere and Cx43 structures, cardiac tissues in eHOC-1.0 condition exhibited an irregular, disorganized sarcomere structure (Fig. 2E and Fig. S5B). We speculate that the highest concentration of GNRs within the eHOC model (1.0 mg/mL) may have disrupted cellular attachment moieties with the hydrogel scaffold, resulting in reduced cell-matrix interaction and subsequently disorganized sarcomere structure. Collectively, these data suggest that although a higher concentration of GNRs resulted in improved electroconductivity of the HOC model, it does not necessarily support structural formation of robust and functional cardiac tissues, emphasizing the necessity of optimization of GNR concentration within the 3D cardiac microenvironment.

### 3.3. *Contractile function of cardiac tissues within eHOC model*

While individual hiCMs are functionally underdeveloped and represent fetal CMs [53], their contractile functionality has been tremendously improved within engineered cardiac tissues *in vitro* [37, 42,54]. Due to observed differences in the sarcomere structure across the designated experimental conditions, revealed by the SAA-stained images, we aimed to assess the influence of the eHOC models on the contractile function of the cardiac tissues. Specifically, we assessed the spontaneous contractile function of the cardiac tissues through beats per minute (BPM), interbeat interval variability (IIV), contraction amplitude, and relaxation time. Cardiac cells started to beat around 2–3 days after injection into the tissue region of the HOC-0.0, eHOC-0.2, eHOC-0.5, and eHOC-1.0 models. However, the beating frequencies of the cardiac tissues evolved over time, and on day 14 of culture, videos were recorded for contractile function analysis. The spontaneous beating patterns of the cardiac tissues are shown in Fig. 3A (Supplementary Video S1). While the beating pattern of cardiac tissues formed within HOC-0.0, eHOC-0.2, and eHOC-0.5 had a regular beating pattern, the cardiac tissues in eHOC-1.0 exhibited irregular contractility. Specifically, quantification of BPM data did not show any significant difference between HOC-0.0, eHOC-0.2, and eHOC-0.5 conditions; however, the cardiac tissues formed in eHOC-1.0 exhibited a significantly lower BPM (Fig. 3B). Notably, while there was no difference in

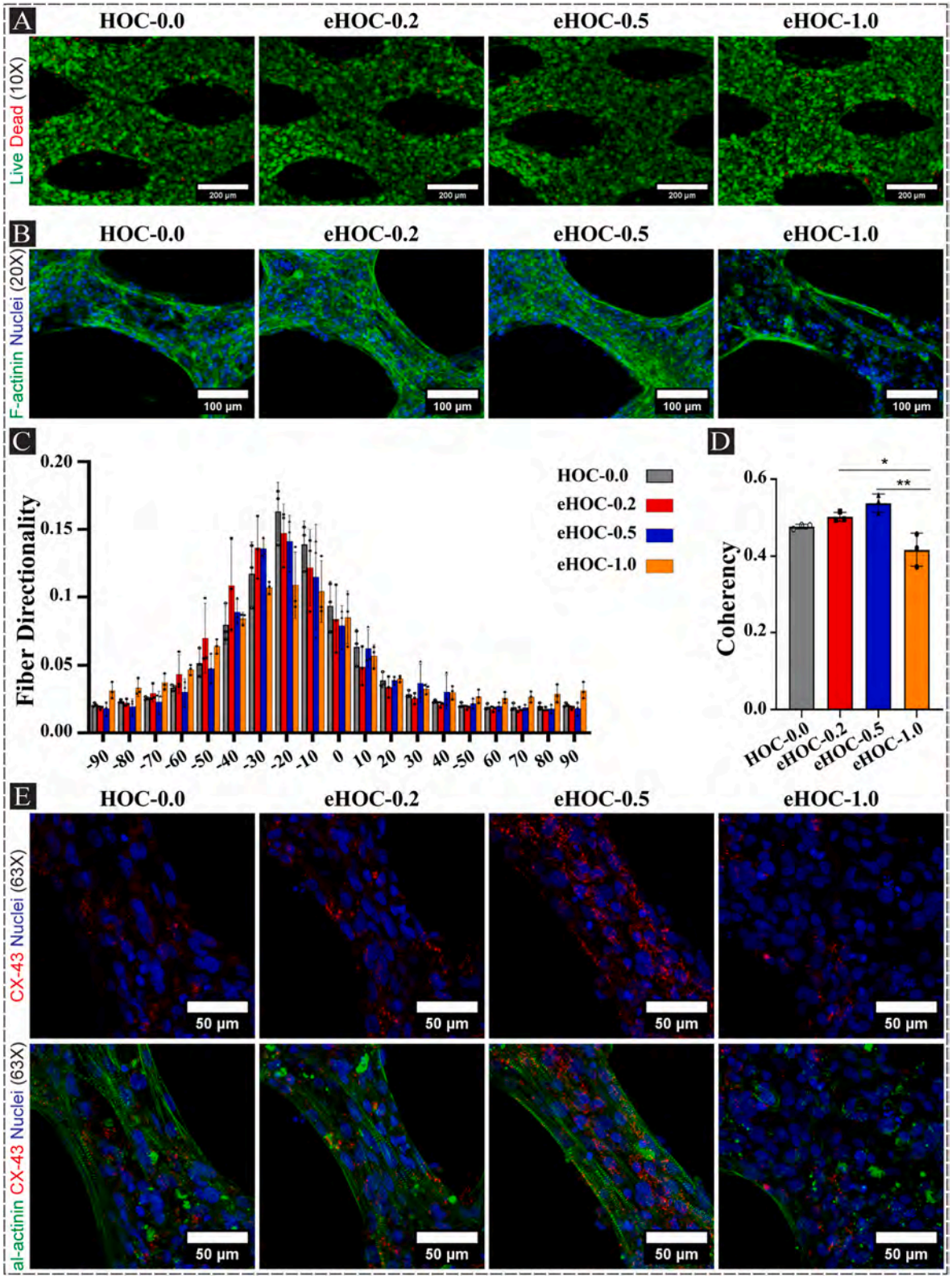


**Fig. 2. Evaluation of cardiac tissues formed within the eHOC model. A**) Viability of cardiac cells cultured within HOC-0.0, eHOC-0.2, eHOC-0.5, and eHOC-1.0 models for 3 days. The scale bar is 200 µm. **B**) IF images of cardiac tissues formed within HOC-0.0, eHOC-0.2, eHOC-0.5, and eHOC-1.0 on day 14, stained for F-actin (green) and nuclei (blue). The scale bar is 100 µm. **C**) Fiber directionality assessment of the F-actin-stained images of the cardiac tissues formed within the HOC models on day 14 of culture. Data were expressed as mean ± standard deviation (n = 3). **D**) Coherency analysis of the cardiac tissues formed in the HOC models. Data were expressed as mean ± standard deviation. *$p < 0.05$ and **$p < 0.01$ (one-way ANOVA with a Tukey's *post-hoc* test, n = 3). **E**) IF images of cardiac tissues formed within HOC-0.0, eHOC-0.2, eHOC-0.5, and eHOC-1.0 models on day 14, stained for alpha-actinin (green), Cx43 (red), and nuclei (blue). The scale bar is 50 µm. (For interpretation of the references to color in this figure legend, the reader is referred to the Web version of this article.)

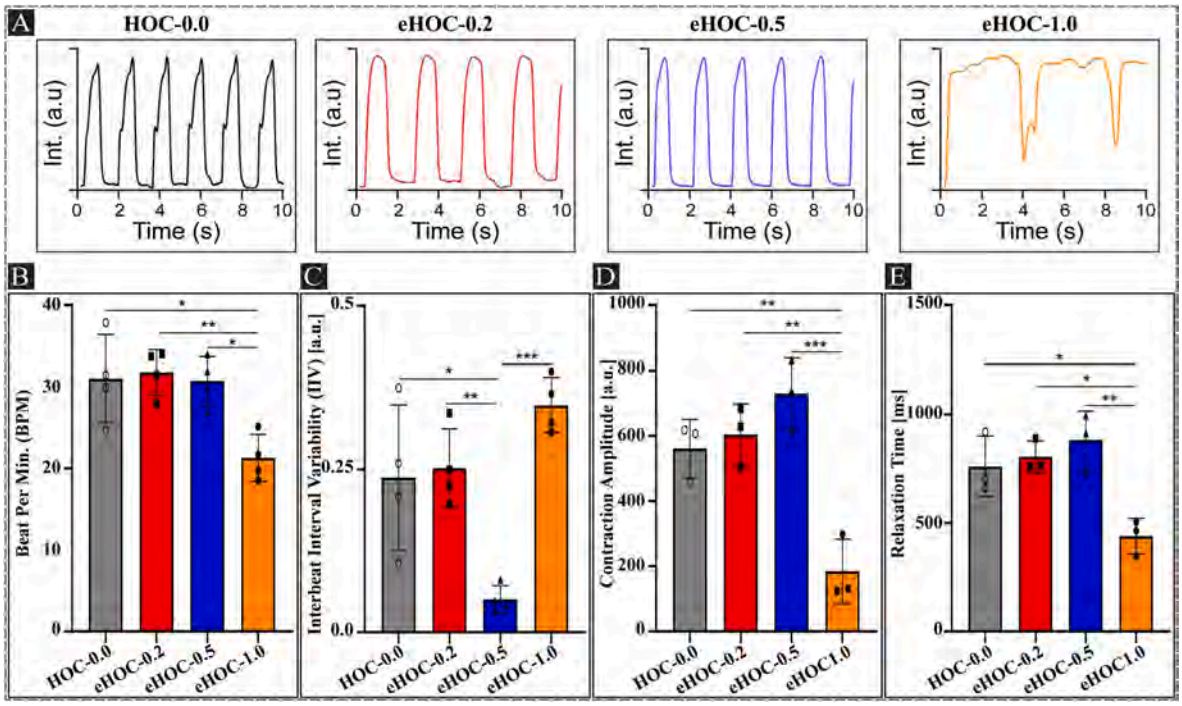


**Fig. 3. Spontaneous contractile function analysis of cardiac tissues formed within the eHOC models. A**) Representative spontaneous beating signal graphs of cardiac tissues formed within HOC-0.0, eHOC-0.2, eHOC-0.5, and eHOC-1.0 on day 14. **B**) Quantitative analysis of the spontaneous beating frequencies of the cardiac tissues showed a significant reduction in beating numbers in the eHOC-1.0 condition compared to the other groups (one-way ANOVA with a Tukey's *post-hoc* test, n = 4). **C**) Spontaneous Interbeat Interval Variability (IIV) showed enhanced beating synchronicity in the cardiac tissues formed within the eHOC-0.5 group (one-way ANOVA with a Tukey's *post-hoc* test, n = 4). **D**) Quantification analysis of the contraction amplitude of the cardiac tissues formed within the HOC model did not show any significant difference between HOC-0.0, eHOC-0.2, and eHOC-0.5, but it was significantly lower in the eHOC-1.0 group (one-way ANOVA with a Tukey's *post-hoc* test, n = 3). **E**) Quantification analysis of the relaxation time of the cardiac tissues formed within the HOC model did not show any significant difference between HOC-0.0, eHOC-0.2, and eHOC-0.5, but it was significantly lower in the eHOC-1.0 group (one-way ANOVA with a Tukey's post-hoc test, n = 3). For B-D, data were expressed as mean ± standard deviation. $*p < 0.05$, $**p < 0.01$, and $***p < 0.001$.

the IIV among HOC-0.0, eHOC-0.2, and eHOC-1.0 conditions, the cardiac tissues formed within the eHOC-0.5 condition exhibited a significantly lower IIV compared to the other experimental groups (Fig. 3C). The significantly lower IIV in the eHOC-0.5 group corresponds to enhanced rhythmic and synchronous contractility of the formed cardiac tissue, potentially, due to the improved development and functional maturation of hiCMs, which facilitated electrical signal propagation. This is also consistent with other studies utilizing electrically active hydrogel scaffolds for cardiac tissue engineering [37,54]. Furthermore, although the contraction amplitude and relaxation time, measured by MUSCLEMOTION plugin software, were not significantly different among HOC-0.0, eHOC-0.2, and eHOC-0.5 conditions, they were significantly lower in the eHOC-1.0 group compared to the other experimental groups (Fig. 3D and E). The reduced contractile functionality of the cardiac tissues formed within the eHOC-1.0 group corresponded well with the disorganized sarcomere structure of the cardiac tissues formed within this condition as shown in Fig. 2E. Consistently, an underdeveloped sarcomere structure has been shown to be associated with nonfunctional contractility in previous study [7]. Additionally, the underdeveloped hiCMs within the eHOC-1.0 condition and reduced cell-cell crosstalk could have resulted in diminished functionality of hiCMs and the overall 3D tissue, causing these cells to beat individually rather than in a synchronized, coordinated, and cohesive manner. Overall, this finding reveals the impact of different degrees of conductivity on the functional aspect of the established cardiac tissue.

Supplementary data related to this article can be found online at https://doi.org/10.1016/j.biomaterials.2025.123275

### 3.4. $Ca^{2+}$ transients of the cardiac tissues formed within the eHOC model

In addition to the importance of an organized and striated sarcomere structure, enhanced electrical coupling of hiCMs is also vital for the formation of functional cardiac tissues [54]. To determine the impact of the eHOC model on the $Ca^{2+}$ handling capabilities of cardiac tissues, changes in intracellular $Ca^{2+}$ levels were monitored using a $Ca^{2+}$-sensing fluorescent dye (Fig. 4 and Supplementary Video S2). $Ca^{2+}$ transient images from at least three regions of interest (ROI) were recorded for each group. The patterns of the $Ca^{2+}$ spikes are shown in Fig. 4A. The cardiac tissues formed in the HOC-0.0 (control) and eHOC-1.0 (high concentration of GNRs) groups exhibited asynchronous calcium flux peaks at different subregions (Fig. 4A). In contrast, a more synchronous calcium flux was observed in the subregions of cardiac tissues formed within the eHOC-0.2 and eHOC-0.5 groups (Fig. 4A). This observation was further confirmed through quantitative analysis of the calcium transients, measured through IIV, which showed significantly lower beating variability for the cardiac tissue, specifically formed within the eHOC-0.5 condition (Fig. 4B). Additionally, further quantitative analysis of the calcium transients revealed that the normalized average change in fluorescence intensity was significantly higher in cardiac tissues formed within the eHOC-0.5 condition compared to other experimental groups (Fig. 4C). The reduced $Ca^{2+}$ flux synchronicity and intensity in the eHOC-1.0 group align well with the contractile function analysis and assessment as demonstrated in Fig. 3. On the other hand, the enhanced $Ca^{2+}$ transient properties of the cardiac tissues within the eHOC-0.5 group could be attributed to the improved development and more efficient coupling of hiCMs. These observations are consistent with recent studies where an electrically active microenvironment utilizing reduced graphene oxide (rGO) [54] and

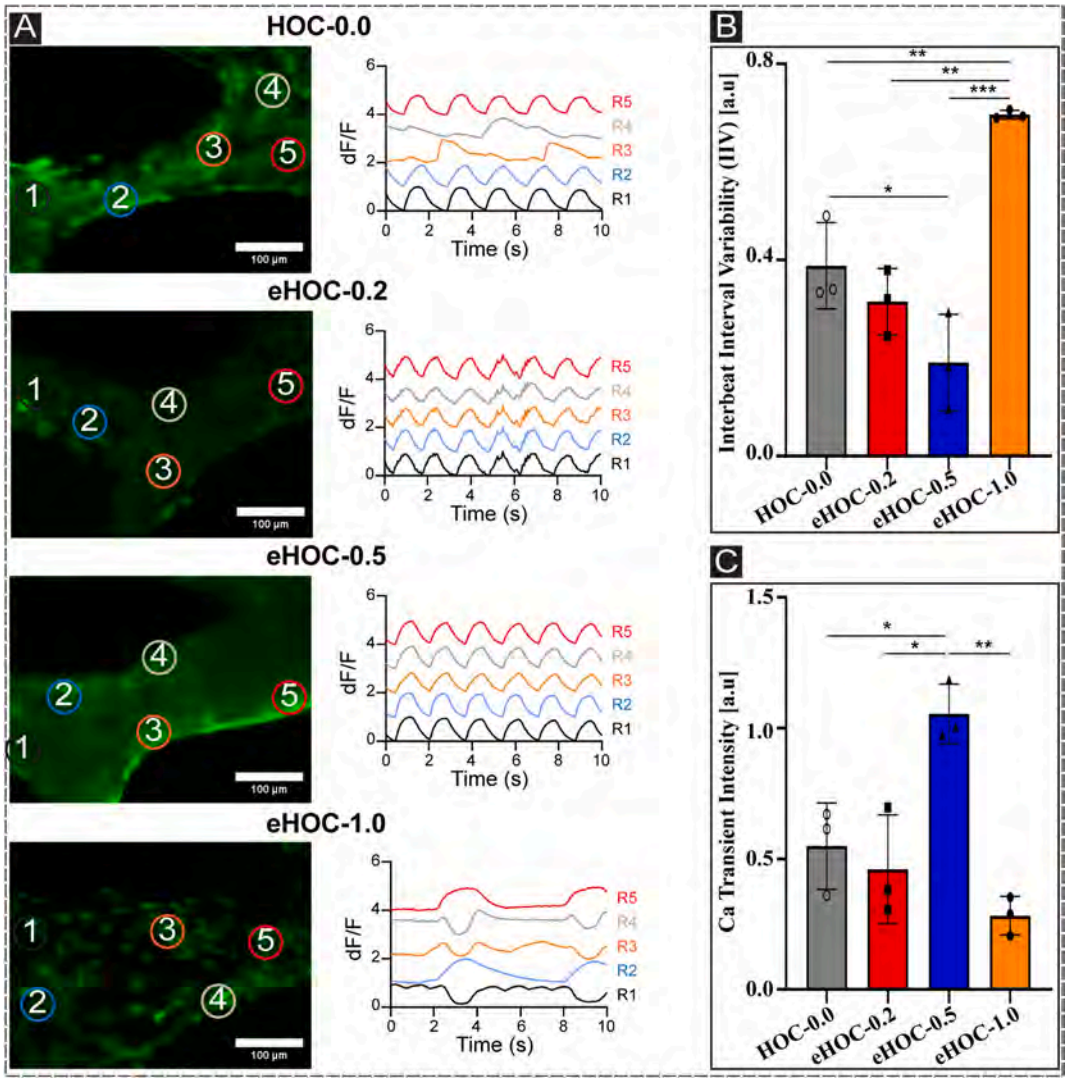


**Fig. 4.** Spontaneous $Ca^{2+}$ transient analysis of the cardiac tissues formed within eHOC model. **A)** Representative calcium transient signals for cardiac tissues formed within HOC-0.0, eHOC-0.2, eHOC-0.5, and eHOC-1.0. Five regions were selected per image, and the correlated signals of each region were shown on the graphs. The scale bar is 100 µm. **B)** IIV data extracted from calcium spikes of cardiac tissues formed within HOC-0.0, eHOC-0.2, eHOC-0.5, and eHOC-1.0 ON day 14 of culture (one-way ANOVA with a Tukey's *post-hoc* test, n = 3). **C)** Calcium transient intensity data extracted from calcium spikes of cardiac tissues formed within HOC-0.0, eHOC-0.2, eHOC-0.5, and eHOC-1.0 at day 14 of culture (one-way ANOVA with a Tukey's *post-hoc* test, n = 3). For B and C, data were expressed as mean ± standard deviation. $*p < 0.05$, $**p < 0.01$, and $***p < 0.001$.

spherical-shaped gold nanoparticles [37] with hiCMs exhibited enhanced $Ca^{2+}$ transient properties within the tissue constructs.

### 3.5. eHOC model improves cardiac gene expression

With the observed enhancement in cardiac tissue contractile and calcium transient functions formed within the eHOC model, we further aimed to assess the expression of cardiac-specific genes using RT-qPCR. Specifically, we examined the expression of genes responsible for ultrastructure (*ACTN2, GJA1, MLC2A, MLC2V, TNNI3, TNNT2, MYH6,* and *MYH7*) and calcium handling (*ATP2A2*, S100A1, *RYR2*, and *CASQ2*) properties [53]. Prior to using hiCMs for the formation of cardiac tissues within the eHOC models, the cells were maintained in supplement/serum-free medium for 24 h to synchronize their cell cycle [55]. The 14-day-old cardiac tissues formed within the eHOC models and an age-matched 2D monolayer control (2D-D14) were compared to a mixture of cells containing the same 4:1 ratio of hiCMs and hiCFs prior to injection into the cardiac tissue channel (referred to as D0). Since the eHOC-1.0 did not lead to the formation of functional cardiac tissue within the chip, this condition was excluded from further biological analysis including gene expression and scRNA-seq.

The gene expression analysis showed that the expression of ACTN2, a sarcomere-related gene in the adult heart [56], was significantly increased in the eHOC-0.5 group compared to 2D-D14 monolayer and HOC-0.0, where there was no change as compared to eHOC-0.2 condition (Fig. 5A). Notably, The *TNNI3* gene, which encodes cardiac troponin I, an essential component of the contractile machinery in adult CMs [53], also exhibited significantly increased expression in the eHOC-0.5 condition compared to eHOC-0.0. The upregulation of these genes aligned well with the collected contractility function data and the cardiac-specific IF images shown in Fig. 3, as *ACTN2* and *TNNI3* regulate the contraction behavior of human CMs [53,56]. Thus, the increased expression of these genes further suggests the enhanced functionality and development of hiCMs within the eHOC-0.5 group. Electrical signal transmission between CMs has been shown to be closely associated with Cx43 gap junction formation [57]. To that end, the expression of the *GJA1*, which codes for this protein, was examined. Notably, *GJA1* gene expression was significantly increased in the eHOC-0.5 group compared

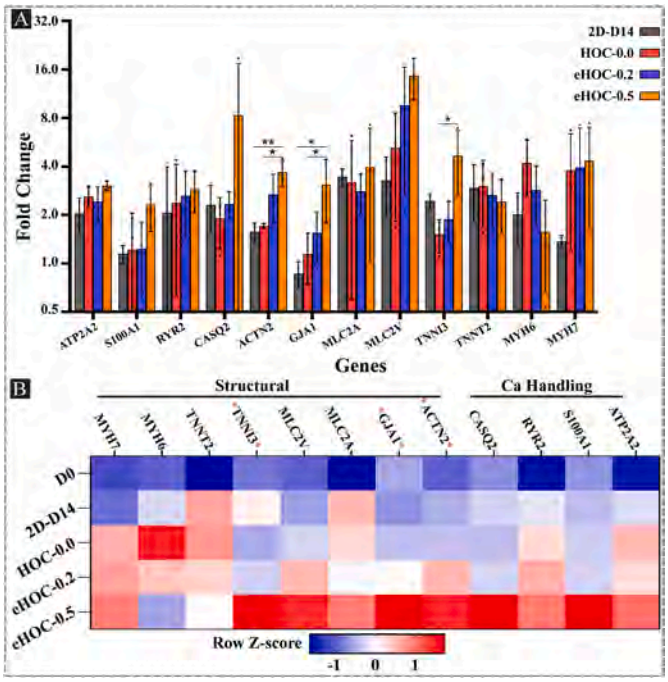


**Fig. 5. Gene expression analysis of cardiac tissues formed within the eHOC model.** hiCMs were exposed to a supplement- and serum-free medium for 24 h before being used for the experiments. hiCMs and hiCFs were encapsulated within the nanoengineered hydrogel scaffolds with a 4:1 ratio, injected into the cardiac tissues channel, and maintained for 14 days before sample collection for gene expression analysis. As a control for gene expression normalization, a portion of hiCMs and hiCFs with the same 4:1 ratio was lysed at Day 0 before injecting into the chips. **A**) Th graph represents the expression of the cardiac structural genes (ACTN2, GJA1, MLC2A, MLC2V, TNNI3, TNNT2, MYH6, and MYH7) and calcium handling genes (ATP2A2, S100A1, RYR2, and CASQ2) in cardiac tissues formed within HOC-0.0, eHOC-0.2, and eHOC-0.5 compared to an aged-matched 2D monolayer condition (2D-D14). Data were expressed as mean ± standard deviation. $*p < 0.05$ and $**p < 0.01$ (one-way ANOVA with a Tukey's *post-hoc* test, n = 3). **B**) The heatmap showing the expression fold changes of structural and calcium handling genes across the culture conditions with z-scores displayed (n = 3).

to 2D-D14 and eHOC-0.0 groups. This observation corroborated well with the enhanced calcium transient properties in the eHOC-0.5 group (Fig. 4), suggesting better coupling of hiCMs within this condition compared to the rest of the experimental groups.

To better observe the overall trend of the cardiac-specific gene expression across the experimental conditions, the Z-scores derived from the average fold changes of the tissues extracted from 2D-D14, HOC-0.0, eHOC-0.2, and eHOC-0.5 groups were plotted in a heatmap as shown in Fig. 5B. Based on the heatmap representation of the data, the expression of the structural-related cardiac genes, *MYH6* and *MYH7*, in the eHOC-0.5 group decreased and increased, respectively. *MYH6* and *MYH7* are both sarcomeric-related genes expressed during heart development with varying expression levels [53]. Specifically, *MYH6* is associated with the early fetal stage, while *MYH7* expression becomes more pronounced during the late stage of heart development [58]. A shift in the expression of *MYH6* to *MYH7* has been shown as a sign of enhanced development of cardiac tissues *in vitro* [59–61]. Examining the gene expression heatmap, it also becomes apparent that the shift from *MYH6* to *MYH7* expression was more pronounced in the eHOC-0.5 group. In addition to the structural-related genes mentioned above, calcium-related genes (*CASQ2*, *RYR2*, S100A1, and *ATP2A2*) also exhibited enhanced expression in the eHOC-0.5 group compared to the HOC-0.0 and 2D-D14 monolayer conditions. These genes, associated with the sarcoplasmic reticulum of CMs, have been reported as major genes upregulated in adult hearts [53]. The increased expression of these genes, aligning well with enhanced $Ca^{2+}$ handling properties of the cardiac tissues, specifically in the eHOC-0.5 group, could further suggest the enhanced development of hiCMs towards an adult stage within our eHOC model system.

### 3.6. scRNA-seq analysis of cardiac tissues formed within the eHOC model

The electrical conduction functional assessments and gene expression analysis revealed that cardiac tissues formed within the 3D eHOC model exhibited improved contractile functionality, $Ca^{2+}$ handling, sarcomere structure, as well as cardiac-specific gene expression. Next, we further performed scRNA-seq to mechanistically identify and characterize distinct transcriptional changes and enriched pathway(s) that may modulate the development of hiCMs within the 3D eHOC model. The overall schematic procedure of the experimental design for scRNA-seq analysis is depicted in Fig. 6A. Cell populations were evaluated from three distinct conditions: a single cell population containing a 4:1 ratio of hiCMs:hiCFs at day 0 before injection into the eHOC model (**D0**), a single cell population extracted from cardiac tissues formed within the 3D **HOC-0.0** (non-conductive control tissue), and a single cell population extracted from cardiac tissues formed within the 3D **eHOC-0.5** (Fig. 6A). Among the electroconductive eHOC groups, the eHOC-0.5 condition was specifically selected for scRNA-seq analysis because this condition resulted in enhanced cardiac tissues function, as indicated by contractility, calcium transient, and gene expression analysis. Additionally, samples from D0 were specifically considered to assess the overall effect of the 3D eHOC model on phenotypic signatures and the development of hiCMs.

Unsupervised clustering identified 12 clusters representing various cell types: undifferentiated hiPSCs, hiCMs, hiCFs, and non-hiCMs/-hiCFs (Fig. 6B). The expression of the pluripotency transcription factor *POUF1 (OCT-4)* was used to identify the undifferentiated hiPSCs. The very low expression of the *POUF1* transcription factor in the identified clusters demonstrated that the hiCMs and hiCFs cell pool used for the scRNA-seq experiments had a minimum (if any) number of undifferentiated hiPSCs (Fig. 6C and Fig. S6A). Based on the presence of the classic CM gene *TNNT2* (cardiac troponin T), almost all the clusters contained hiCMs (Fig. 6C and Fig. S6A). Considering that hiCFs were a major population in our culture system, these cells predominantly appeared in 4 clusters (clusters 6, 8, 9, and 10), specifically identified by the presence of fibroblasts gene markers *VIM, POSTN, DDR2, THY1, FAP*, and *FN1* (Fig. 6C and Fig. S6A). In some cases, cells presented multiple classical marker genes associated with hiCMs and a secondary cell type within the same cluster. For instance, in cluster 8, *TNNT2*$^{+}$ hiCM-like cells were observed, and these cells also expressed TRPM3 (smooth muscle cell-like marker) (Fig. 6C and Fig. S6A). However, this observation is consistent with the *in vitro* differentiation protocols of hiCMs and hiCFs reported in other studies, where various cell types are typically generated within the same batch of differentiation [58,62,63]. In summary, a total of 5871 cells were captured, of which 5789 cells were retained after quality control analysis (Figs. S6B and C).

Next, differentially expressed genes (DEGs) analysis was performed to assess the overall impact of 3D HOC-0.0 and eHOC-0.5 models on dysregulated genes compared to D0. The analysis revealed a significant transcriptional shift between the hiCMs from D0 and hiCMs from both 3D HOC-0.0 and eHOC-0.5 groups (Fig. 6D). For the rest of the analysis, we primarily compared 3D groups (combined HOC-0.0 and eHOC-0.5) with the D0 group to examine the effects of 3D culture condition on the development of hiCMs. Particularly, we identified a total of 6 different hiCMs clusters from our cluster analysis. To gain further insights in the expression pattern across different clusters, we compared the DEGs of identified hiCMs against 2D (Fig. 6E), which revealed the presence of different DEGs across various clusters, reflecting a subpopulation-specific changes within the hiCMs (Fig. 6E). Complementing this, comparing the distribution of gene expression levels for the top DEGs across each identified cluster, revealed a variability across

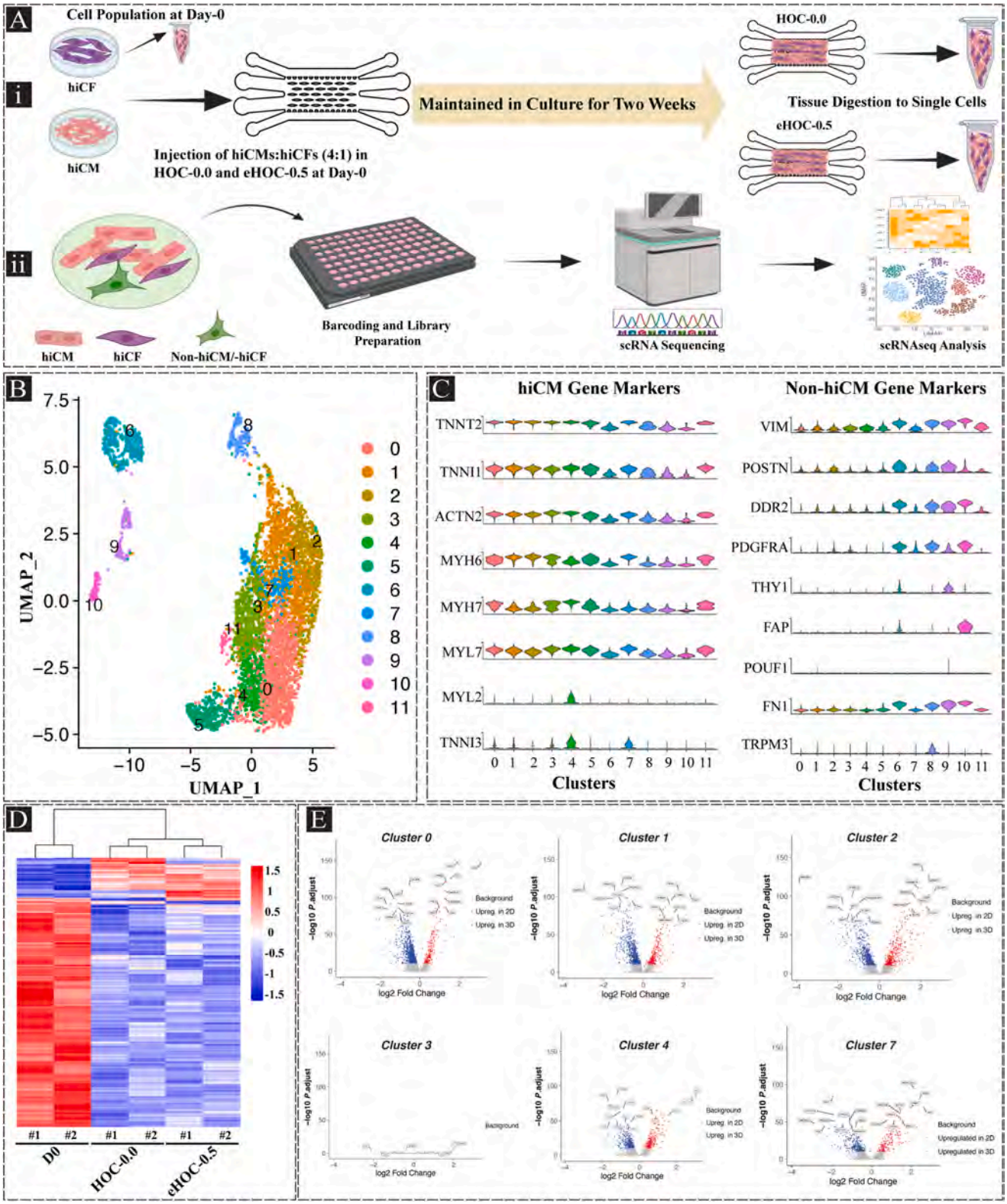


**Fig. 6. Single-cell transcriptomic analysis of hiCMs extracted from cardiac tissues formed within the 3D HOC model. A**) Single-cell RNA sequencing (scRNA-seq) schematic highlighting the collection of singularized cardiac cells from D0, HOC-0.0, and eHOC-0.5 experimental groups followed by scRNA-seq analysis. Created with BioRender.com **B**) UMAP plot illustrating 12 clusters. Cluster IDs were assigned after clustering based on cluster size, with cluster 0 containing the most cells and cluster 11 containing the least. **C**) Violin plots indicating normalized transcript abundance of cell type marker genes by cluster. **D**) Differentially expressed genes were identified between D0, HOC-0.0, and eHOC-0.5. The heatmap indicates the transcriptional shift between hiCMs at D0, and hiCMs extracted from the 3D conditions (i.e., HOC-0.0 and eHOC-0.5) at day 14 of culture. **E**) Volcano plot illustrating the differentially expressed genes of hiCMs between 3D and 2D, analyzed for identified hiCMs clusters. Log2 fold change (log2FC) $> 0$ indicates upregulated genes in the hiCMs in 3D and log2FC $< 0$ indicates upregulated genes in the hiCMs in 2D. *Red: upregulated genes in 3D (p. adjust* $< 1e^{-10}$*), Blue: downregulated genes in 3D (p. adjust* $< 1e^{-10}$*).* (For interpretation of the references to color in this figure legend, the reader is referred to the Web version of this article.)

each cluster with distinct expression pattern (Fig. S6D). Together, these findings emphasize the transcriptional diversity within the identified cell clusters.

Next, combing the biological replicates together (Fig. 7A), we observed a similar trend in transcriptional changes across the different conditions. By comparing D0 and 3D hiCM samples, we identified a total of 1895 significantly expressed DEGs (adjusted P value < 1e-10, excluding mitochondrial genes), of which 275 were upregulated and 1620 were downregulated in the 3D HOC model compared to D0 samples (Table S3). The volcano plot in Fig. 7B**(i)** shows changes in the gene expression profile in response to 3D culture conditions, highlighting significant DEGs. Specifically, the expressions of *FHL2*, *NFIA*, *A2M*, *MYL9*, *KCNQ1*, and *TNNI3K* were significantly upregulated in the 3D conditions. In addition to the upregulation of cardiac maturation genes, the analysis revealed a significant downregulation of cardiac fetal-like genes, including *HAND1*, *APOE*, *COL2A1*, *MYL3*, and *CLDN6* (Fig. 7B **(i)**). This trend aligns and is consistent with recent studies, where early-stage hiCMs were found to be enriched for the expression of *APOE*, *COL2A1*, *CLDN6*, and *MYL3* [58].

Further, eHOC-0.5 was then compared directly with HOC-0.0 (i.e. non-conductive control tissue), to further delve into the impact of electroconductivity features of the tissue microenvironment on the transcriptomic profile of the cultured hiCMs. In comparison with D0 *vs.* 3D, a smaller number of significant DEGs were found when comparing eHOC-0.5 to HOC-0.0, with specifically 48 genes upregulated and 7 downregulated (Table S4), as highlighted in Fig. 7B**(ii)**. Notably, key cardiac sarcomeric genes, including *TNNT2*, *TTN*, *MYPBC3*, and *MYL6*, crucial for sarcomere assembly [7], were upregulated in eHOC-0.5. This aligns with the results of a recent study where these genes showed upregulation in 3D hiPSC derived cardiac microtissues [7].

To delve deeper into the transcriptional changes in the established cardiac tissue in the presence of nanoengineered electrically conductive scaffold, we performed a DEG analysis by comparing the expression levels of a panel of selected marker genes associated with cardiac tissue structure (structural genes – Fig. 7C**(i)**) as well as tissue function (conduction- Fig. 7C**(ii)** and calcium handling – Fig. 7C**(iii)**) across the three experimental conditions. Comparison of structural genes across conditions revealed the upregulation of ultrastructure genes, namely *MYH6, TNNI3,* and *TNNT2* particularly in eHOC-0.5 (Fig. 7C**(i)**), underscoring the positive impact of the presence of GNRs in tuning the structural organization of the established tissue within the HOC model system [18]. Of note, *TNNI1*, a gene that plays a crucial role in the maturation of CMs during development, was found to be co-expressed in the hiCMs from eHOC-0.5, underscoring the developmental stage of hiCMs within our model [64]. Importantly, we also observed the upregulation of conduction genes such as *KCNH2*, *KCNQ1*, *HCN1* and down-regulation of *HCNC4* in eHOC-0.5, confirming the enhanced cardiac tissue conductivity. These findings are consistent with previous studies [65]. Furthermore, genes such as *CAV3* and *RYR2,* which participate in calcium handling, were found to be upregulated in eHOC-0.5, underscoring the presence of hiCMs with adult-like behavior, consistent to previous study [65]. Based on these analyses, hiCMs within the 3D eHOC-0.5

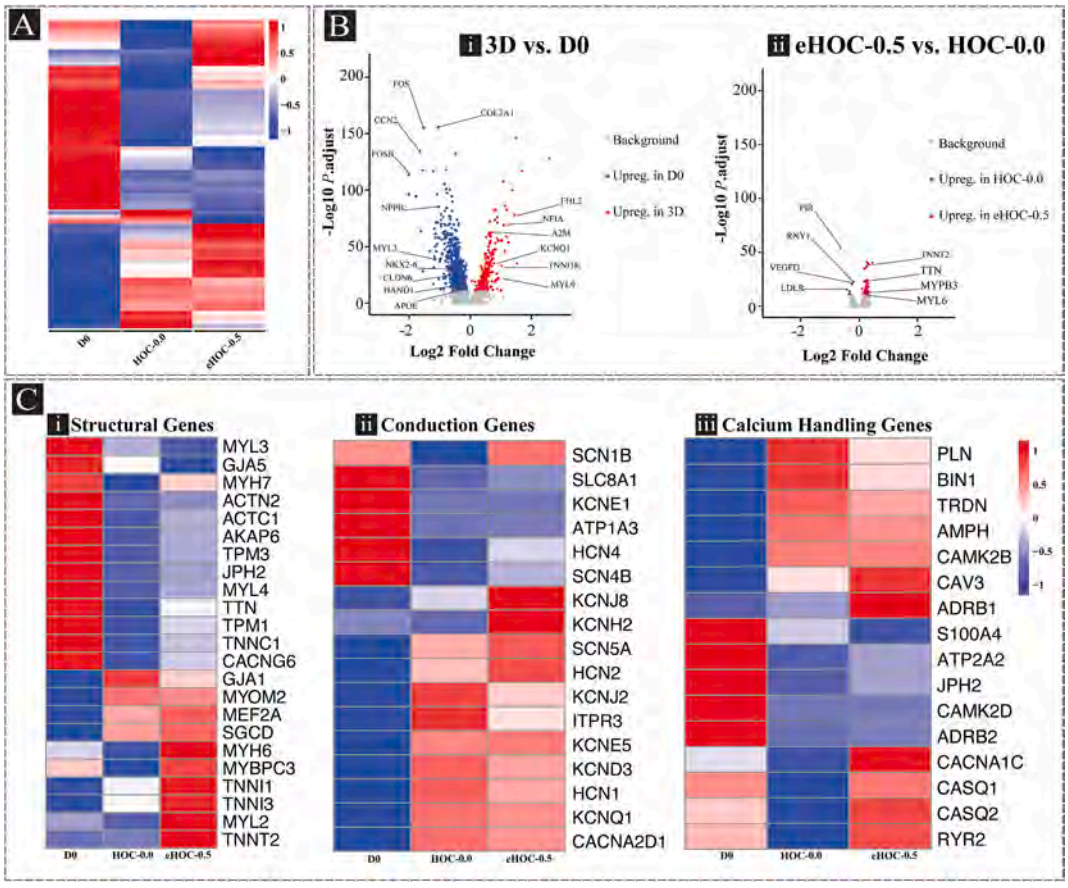


**Fig. 7. Expanded scRNA-seq analysis of differentially expressed genes of the cardiomyocytes. A**) Heatmap depicting the transcriptomic differences of hiCMs across the experimental conditions, excluding low-expressed genes. Heatmap color represents the Z-score transformed expression level. **B)** Volcano plots display differential expression of genes between 3D and D0 (**i**) and HOC-0.0 and eHOC-0.5 (**i**). Log2 fold change (log2FC) > 0 indicates upregulated genes in the hiCMs in 3D versus D0 (**i**) and eHOC-0.5 versus HOC-0.0 (**ii**), whereas log2FC < 0 indicates upregulated genes in the hiCMs in D0 versus 3D (**i**) and HOC-0.0 versus eHOC-0.5 (**ii**). The selected top genes are annotated on the volcano plots. *Red: upregulated genes in 3D (p. adjust* < $1e^{-10}$*), Blue: downregulated genes in 3D (p. adjust* < $1e^{-10}$*)* **C**) Heatmap of differential expression of selected structural (**i**), conduction (**ii**), and calcium handling genes (**iii**). Heatmap color represents the Z-score transformed expression level. (For interpretation of the references to color in this figure legend, the reader is referred to the Web version of this article.)

displayed further improvement in terms of the upregulation of key structural genes, conduction and calcium handling genes potentially suggesting the positive impact of the electrical conductivity on cardiac tissue function, maturation and structural organization toward an adult phenotype. Furthermore, regardless of the electroconductivity, in addition to the upregulation of genes associated with the adult stage, cardiac fetal genes were also downregulated when hiCMs cultured within the 3D tissue environment of the HOC model.

An important aspect of our study was to investigate the enriched pathway(s) involved in the development and maturation of hiCMs within the engineered eHOC model. Using Kyoto Encyclopedia of Genes and Genomes (KEGG) database, we first assessed the significantly enriched pathways in 3D culture systems versus D0 samples, revealing that a total of 16 and 11 pathways were upregulated and downregulated, respectively as shown in (Fig. 8A**(i)**). Notably, the calcium signaling pathway appeared to be significantly upregulated in the 3D HOC model. The pathway gene network analysis further revealed that genes, including *PDE1C, ITPR2, ITPKB, P2RX1, CHRM2, GRM1, RYR3,* and *HRH2*, important for calcium handling in hiCMs, were involved in this upregulated pathway (Fig. 8A**(ii)**). Additionally, pathways such as neuroactive ligand-receptor interaction, protein digestion and absorption, glutamatergic synapse, and cell adhesion molecules were upregulated, while pathways including cell cycle, FoxO signaling pathway, and hypertrophic cardiomyopathy were downregulated, consistent with other studies [7]. The upregulation of the glutamatergic synapse, which plays a significant role in vital cardiac functions such as rhythm and excitation of CMs [66,67], implies the positive impact of the 3D tissue formation within the microfluidic HOC model on hiCM development. Admittedly, genes including KCNQ1 and RYR3 important for $Ca^{2+}$ handling and contraction [53], were also found to be upregulated across the pathways.

When comparing eHOC-0.5 to HOC-0.0 to assess the impact of electroconductivity on pathway enrichment, sarcomere-related genes such as *TNNT2* were enriched in cardiac muscle contraction pathway in the eHOC-0.5 group (Fig. 8B**(i)**). During muscle contraction, myosin, a motor protein, and the filamentous actin protein form cross-bridges, allowing myosin to slide along actin, leading to length changes and force generation [68]. Here, myosin-related genes, including *MYH6, MYL12A, and MYL6*, were shown to be enriched in the motor protein pathway (Fig. 8B**(ii)**).

The metabolic switch from glycolysis in early-stage hiCMs to fatty acid oxidation in late-stage hiCMs has been previously reported [69]. While the fatty acid oxidation genes did not get upregulated, the genes associated with glycolysis were downregulated in the 3D HOC models (Fig. S7). However, the dysregulated genes did not enrich in a metabolically related signaling pathway. Collectively, calcium handling and sarcomere-related genes, identified through DEGs analysis, appeared to be enriched in calcium handling and cardiac muscle contraction pathways consistent with the functional assessments performed earlier.

To further investigate and validate the physiological relevance and biomimicry of the 3D eHOC-0.5 model, we assessed the level of hiCM development derived from our model relative to *in vivo* human heart development. To that end, we compared the significant DEGs from the D0, HOC-0.0, and eHOC-0.5 samples with DEGs obtained from RNA-seq data of fetal and adult hearts in ENCODE [70] (Fig. 9). In total, we found 160 common DEGs between our dataset and the published dataset of the human samples (Table S5). To draw an analogy between our model and *in vivo* heart development, we converted the CPM-normalized bulk expression matrix and single-cell expression matrix into log2 scale, followed by Z-score normalization, and plotted them in separate heatmaps. The analysis showed that expression of approximately 65 % of DEGs between D0 to 3D HOC models correlated with the same pattern as the changes of 91-fetal state to adult state, as highlighted in black dotted rectangular boxes shown in Fig. 9. Collectively, these data suggest that hiCMs in the 3D HOC model represent a more developmentally mature state compared as to hiCMs at D0 condition (in the absence of the 3D HOC and conductive environment).

## 4. Discussion

Engineering biomimetic and physiologically relevant *in vitro* models of human cardiac tissues has been the center of attention in the field in the past few years. When aiming to closely replicate the myocardial niche, it is crucial to incorporate a 3D culture microenvironment, within *in vitro* model systems, to better emulate the structural organization of cell-cell and cell-matrix components [71]. Several approaches, including cardiac organoids and engineered heart tissues (EHTs) based on the combination of hiCMs and biomaterials, have been widely utilized to replicate *in vivo* heart tissues [10,65]. Over the past few years, microfluidic-based Heart-on-a-Chip (HOC) models have emerged as promising technology platforms to engineer biomimetic 3D human myocardial-like tissues, with precise features at a micro-scale level and establishing microenvironments conducive to enhanced functionalities of hiPSC-derived cardiac tissues. While various HOC models with specific novelties have been developed [13,16,18,42,72,73] thus far, the majority of the previously reported models lack the electrical conductivity (i.e. electroconductivity) features that native heart tissues possess. To address this, in this work, we hypothesized that integrating electroconductivity cues into an anisotropic microfluidic-based HOC model will provide more biomimetic and physiologically relevant hiPSC-derived cardiac tissues with enhanced functionalities, phenotype, and genetic signatures.

We specifically developed an electroconductive HOC model (eHOC), incorporating various concentrations of gold nanorods (GNRs) embedded within a cocktail of Collagen-I: Matrigel hydrogel matrix. The experimental conditions were specifically designated as HOC-0.0 (non-conductive control), eHOC-0.2 (0.2 mg/mL GNRs), eHOC-0.5 (0.5 mg/mL GNRs) and eHOC-1.0 (1.0 mg/mL GNRs). Notably, the cardiac tissues formed within the eHOC-0.5 microenvironment exhibited improved contractile function and calcium transient features. RT-qPCR analysis of a set of key cardiac genes demonstrated that the enhanced functional properties of the cardiac tissue coincided with the upregulation of calcium handling and structural genes. Notably, *GJA1*, *TNNI3*, and *ACTN2* were all significantly upregulated in the eHOC-0.5 condition. These observations align well with other previous studies where enhanced contractile function and increased expression of genes associated with the contractile machinery were observed in cultured hiCMs encapsulated within gold nanoparticle-incorporated hydrogel scaffolds [37] or alternatively a decellularized ECM structure decorated with reduced graphene oxide (rGO) [54].

It is worth mentioning that the modulation of cardiac tissue environment, through the incorporation of electroconductive elements, could also alter structural and biophysical features of the tissue. Along this line of thought, as demonstrated in previous studies, the change in tissue stiffness due to the incorporation of GNRs was suggested as a potential mechanism for improved cardiac tissue function [38,50]. However, in a recently published study using rGO [54], along with an electroconductive hydrogel group, a non-conductive group with similar stiffness was also designed to dissect the potential role of electroconductivity of the hydrogel matrix and the introduced stiffness, due to the presence of the conductive component, on cardiac tissue function. Notably, it was demonstrated that the relative expressions of various ion channels and *GJA1* gene in the stiffness-matched group were lower than those in the electroconductive group. It was speculated that tissue microenvironment stiffness appears to exert a limited effect on regulating this subset of electrophysiological development [54]. Other mechanisms have been also suggested by which electroconductive microenvironments enhance the functionality of cardiac tissues *in vitro* [74–76]. It has been speculated that the electroconductive components reduce the electrical resistance of the porous scaffolds [30], working as a wire to propagate the ionic currents from the beating cardiomyocytes, facilitating cell-cell crosstalk [27]. In our study, we also demonstrated

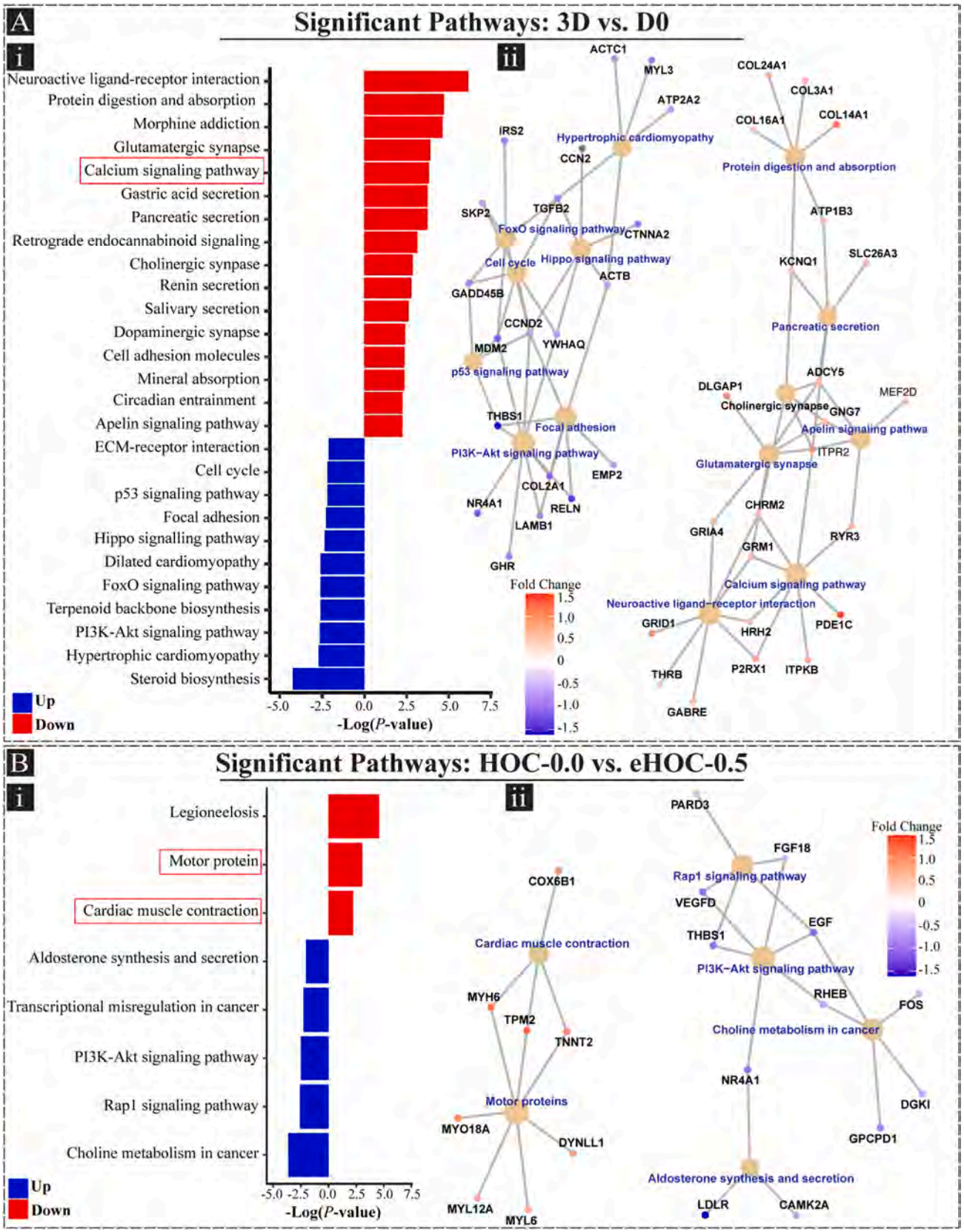


**Fig. 8. Pathway enrichment analysis of the cardiac tissues formed within the HOC model. A**) Pathway analysis shows enriched pathways in downregulated (blue) and upregulated (red) genes in 3D compared to D0 (left plot) with $p$-value <0.01. The right plot displays the enriched genes in the top pathways. **B**) Pathway analysis shows enriched pathways in downregulated (blue) and upregulated (red) genes in eHOC-0.5 compared to HOC-0.0 (left plot) with $p$-value <0.01. The right plot displays the enriched genes in the top pathways. (For interpretation of the references to color in this figure legend, the reader is referred to the Web version of this article.)

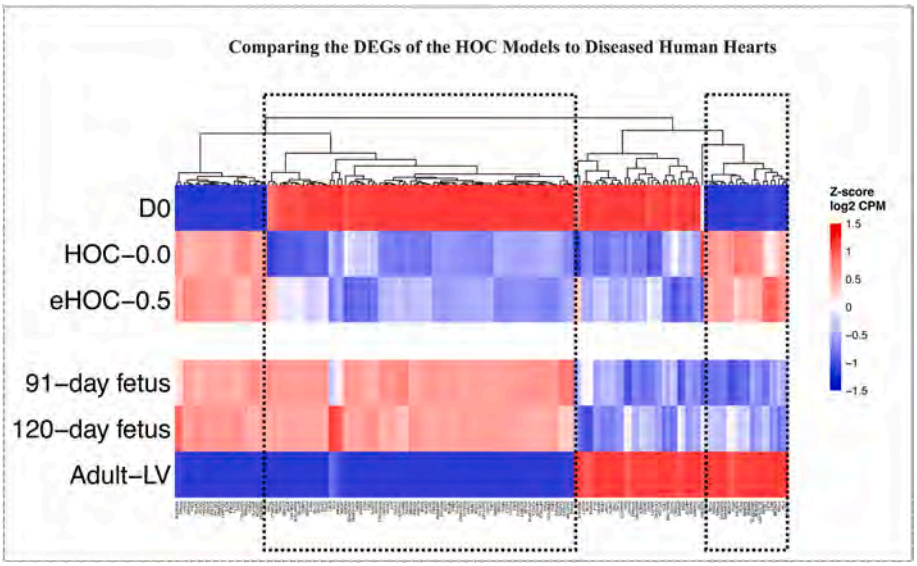


**Fig. 9.** Comparison of DEGs from the 3D HOC models with the published datasets from human samples. The top panel shows the differences in gene expression levels among D0, HOC-0.0, and eHOC-0.5. The bottom panel displays the differences in gene expression levels among the 91-day fetus heart sample, 120-day fetus heart sample, and adult LV sample. The expression levels have been standardized using Z-score. The genes highlighted in the black boxes show similar expression changes from D0 to the 3D HOC model and from fetus to adult LV.

that the electroconductive microenvironment, embedded within the HOC model (eHOC), enhanced the expression of sarcomere-related genes and proteins of the cardiac tissues, likely resulting in better cardiac tissue function. Considering all the previous literature including our own work, to better unveil the specific contribution of electroconductive materials or nanomaterials on cardiac tissue function, further mechanistic and in-depth studies need to be undertaken. While bulk RNAseq analysis has been performed on hiPSC-derived cardiac tissues embedded within electroconductive microenvironments through random encapsulation of the cells within the hydrogel matrix [37], none of the previous studies have utilized a more advanced mechanistic approach, namely scRNA-seq analysis, within a structurally biomimetic and electrically conducive tissue environment, resembling the native human myocardium, to mechanistically delve into the action of conductive elements (i.e., GNRs) on the enhanced functionalities and phenotype of cardiac tissues.

In this study, we conducted scRNA-seq analysis of cardiac tissues integrated with our eHOC model to further analyze the unbiased transcriptomic profiles of the tissue at single-cell level in response to the 3D tissue environment and electroconductive GNRs and to assess the biomimicry of our model (eHOC-0.5 model) relevant to human myocardial tissue. Our analysis showed that hiCMs from both the 3D HOC-0.0 and eHOC-0.5 models exhibited a distinct transcriptional shift compared to hiCMs from D0 condition (i.e., prior to injection into the chip). Stage-specific transcriptomic analysis of *in vitro* differentiated hiCMs revealed the downregulation of fetal genes and upregulation of adult genes at three months post-differentiation [58,69]. In this work, regardless of the electroconductivity features of the 3D HOC models, we observed a trend where the expression of cardiac genes associated with the early stage and late stage of hiCM differentiation were found to be significantly downregulated and upregulated, respectively. Furthermore, analysis of the significantly DEGs in the 3D conditions revealed that *COL2A1, FOS, FOSB*, and *CCN2* were among the top downregulated genes. *FOS* and *FOSB* belong to the *FOS* gene family, are regulators of cell proliferation, and their upregulation has been reported in heart failure [77]. *CCN2* (known as connective tissue growth factor; CTGF), a cysteine-rich, matrix-associated, secreted protein [78], is repressed in healthy hearts after birth and induced in heart failure [79]. Given that these genes have been shown to exhibit a higher expression level in human fetal hearts compared to adult hearts [70], their downregulation in our study potentially implies the development of hiCMs toward an adult state in our 3D HOC model system. Notably, the 3D HOC model displayed the upregulation of genes involved in $Ca^{2+}$ handling and cardiac contraction, including *KCNQ1*, *TNNI3K*, and *MYL9*. Similar to another study where the downregulation of *MYL3* and upregulation of *MYL9* have been reported in late-stage differentiated hiCMs (90 days old) [69], the same trend was also observed in our study where *MYL3* and *MYL9* were significantly downregulated and upregulated respectively in our 3D HOC model compared to the D0 group. Altogether, these findings suggest the development and maturation of hiCMs in our 3D tissue model system. Interestingly, a side-by-side comparison of the HOC-0.0 and eHOC-0.5 models revealed the distinct role of electroconductivity on the transcriptomic profile of hiCMs. Importantly, upregulation of sarcomeric-related genes, including *TNNT2*, *TTN*, *MYBPC3*, and *MYL6*, was observed in the eHOC-0.5 model due to the presence of electrically conductive GNRs within the 3D tissue model. Overall, the DEGs analysis through scRNA-seq supported the enhancements observed in the functionality of the cardiac tissues in the eHOC-0.5 model due to the presence of the 3D environment as well as electrically conductive features.

Although there is an abundance of examples demonstrating that electroconductive scaffolds enhance the functionality of hiCMs and NRVMs [35], the signaling pathways mediated by these types of materials have yet to be fully elucidated. In almost all reported cases, the most significant improvements in performance were observed in parameters related to electrical coupling, such as Cx43/*GJA1* expression [54]. KEGG enrichment analysis in our study demonstrated that the DEGs were enriched in a myriad of pathways. Notably, when comparing the 3D HOC models against D0 experimental condition, the calcium signaling pathway was significantly upregulated. The enrichment of this pathway aligns well with the observed improved $Ca^{2+}$ properties of the cardiac tissues demonstrated above. It is worth noting that signaling pathways associated with human heart diseases, including hypertrophic cardiomyopathy, aldosterone synthesis and secretion [80], PI3K-Akt signaling pathway [81], as well as Rap1 signaling pathway [82], were downregulated in our 3D HOC and eHOC models. However, when comparing eHOC-0.5 against HOC-0.0 to specifically assess the effect of electroconductivity feature of the tissue (i.e. due to presence of GNRs) on pathway enrichment, the cardiac muscle contraction and motor protein pathways were found to be significantly upregulated. This

observation was consistent with a recent study where electroconductive microenvironments showed enrichment in the muscle contraction pathway [37]. Interestingly, the PI3K-Akt signaling pathway, and the aldosterone synthesis and secretion pathway were also downregulated in the electroconductive GNR-incorporated HOC model (eHOC), necessitating future studies to uncover the potential role of electroconductivity in downregulation of these subsets of cardiac pathways.

After birth, the human CMs become more developmentally mature compared to their fetal forms, and their metabolism depends on fatty acid oxidation rather than glycolysis [53]. While the gene profile associated with fatty acid oxidation did not significantly change in our HOC models (either HOC-0.0 or eHOC-0.5), the genes associated with glycolysis metabolism, including *SLC2A3, PDK1, PGAM1, HK2, PFKP*, and *GLUD1* were significantly downregulated in hiCMs cultured in the 3D HOC models. The reduced expression of these genes has also been reported in hiCMs cultured in a cardiac organoid model [7]. This reduced expression of fetal-like metabolism genes within our 3D HOC models could imply that the hiCMs were more metabolically developed compared to the hiCMs at D0. However, further studies, such as an extended culture time of hiCMs within the 3D eHOC-0.5 model, are required to assess the expression trend of metabolic genes associated with adult stage longer period of culture time.

One of the important criteria for the development of reliable *in vitro* cardiac models is how and to what extent they mimic the CMs from native tissues. In-depth molecular-level studies, such as RNAseq, specifically scRNA-seq, has enabled us to directly compare the transcription profile of *in vitro* cardiac tissues to published data sets from *in vivo* human samples. A recent study reported that the 30-day-old differentiated hiCMs were more representative of a fetal stage than the adult stage [63]. In our study, notably, we demonstrated a similar transition trend, when comparing the normalized 3D HOC model data to D0 and the adult LV to 91-day fetus samples from the published literature (i.e., 60 % of gene expression transformations). Despite the similarities between the expression patterns of cardiac genes in the 3D eHOC-0.5 model with the adult human LV, some transcriptome profiles were still different, suggesting the need for further improvements in *in vitro* microenvironments to enhance the biomimicry of cardiac tissues. Specifically, additional considerations could include the integration of electromechanical cues [65], metabolites and hormones [73], extended culture time [69], and making the model more complex by co-culture of other cell types, such as endothelial cells [7], into our 3D eHOC-0.5 model, which will be the subject of our future studies.

## 5. Conclusion

In this study, we developed a 3D electroconductive HOC (eHOC) model by integrating nanoengineered electroconductive hydrogel scaffolds within a microfluidic-based model system for generation of biomimetic hiPSC-derived cardiac tissues. The 3D eHOC model demonstrated enhanced calcium transient features and improved contractility function. Furthermore, molecular analysis of the cardiac tissues through RT-qPCR also confirmed the increased expression of structural and calcium handling genes in the 3D eHOC model supporting the observed functional improvements. The biomimicry of the developed model was further investigated through scRNA-seq analysis. The DEG analysis showed that, in addition to the downregulation of fetal-associated cardiac genes, adult-state cardiac genes were upregulated in the 3D eHOC model. We demonstrated that, regardless of the electroconductivity cues, the 3D HOC model displayed the enrichment of the calcium handling pathway. However, when comparing the 3D eHOC-0.5 versus HOC-0.0, the cardiac contraction and motor protein pathways were significantly upregulated, demonstrating the positive impact of electroconductive cues on this subset of molecular mechanisms. Notably, the improved calcium handling, cardiac contractile pathways, and motor protein pathways align well with the observed enhancements in cardiac tissue function. Finally, by comparing our data set against the published dataset of adult and fetus hearts, we demonstrated that the transition from a fetal stage in D0 samples to a more functional hiCM in the 3D eHOC-0.5 model was similar to the same pattern observed during heart development from fetus to adult stage. In summary, this study serves as a fundamental step for engineering more biomimetic hiPSC-derived cardiac tissues within 3D eHOC models and potentially serves as a reliable platform for future disease modeling and drug testing studies.

## CRediT authorship contribution statement

**Hamid Esmaeili:** Writing – review & editing, Writing – original draft, Visualization, Validation, Methodology, Investigation, Formal analysis, Data curation, Conceptualization. **Yining Zhang:** Formal analysis. **Kalpana Ravi:** Methodology. **Keagan Neff:** Methodology. **Wuqiang Zhu:** Writing – review & editing. **Raymond Q. Migrino:** Writing – review & editing. **Jin G. Park:** Writing – review & editing, Formal analysis. **Mehdi Nikkhah:** Writing – review & editing, Supervision, Resources, Project administration, Methodology, Funding acquisition, Conceptualization.

## Declaration of competing interest

The authors declare the following financial interests/personal relationships which may be considered as potential competing interests: Mehdi Nikkhah reports financial support was provided by National Science Foundation. Mehdi Nikkhah reports financial support was provided by National Institutes of Health. Wuqiang Zhu reports financial support was provided by National Institutes of Health. If there are other authors, they declare that they have no known competing financial interests or personal relationships that could have appeared to influence the work reported in this paper.

## Acknowledgment

The authors would like to thank the National Science Foundation (NSF) CBET Nanoscale Interactions Program Award # 2016501 (MN) and NIH NHLBI Award # 1R01HL172784-01 (MN and WZ) for financially supporting this project. The authors would also like to acknowledge Prof. Barbara Smith for providing qTower 2.0 access for qPCR analysis, Prof. Jennifer Christen for providing us with the EIS set up for Impedance measurement, Yamini Singh and Ronin-Mae Komarnisky for performing the SEM imaging and mechanical characterization of the nanoengineered hydrogel scaffolds, and Prof. Juliann Holloway for assisting in compressive modulus measurement.

## Appendix A. Supplementary data

Supplementary data to this article can be found online at https://doi.org/10.1016/j.biomaterials.2025.123275.

## Data availability

Data will be made available on request.

## References

[1] C.W. Tsao, A.W. Aday, Z.I. Almarzooq, A. Alonso, A.Z. Beaton, M.S. Bittencourt, A. K. Boehme, A.E. Buxton, A.P. Carson, Y. Commodore-Mensah, Heart disease and stroke statistics—2022 update: a report from the American Heart Association, Circulation 145 (8) (2022) e153–e639.
[2] B. Fine, G. Vunjak-Novakovic, Shortcomings of animal models and the rise of engineered human cardiac tissue, ACS Biomater. Sci. Eng. 3 (9) (2017) 1884–1897.
[3] K. Takahashi, S. Yamanaka, Induction of pluripotent stem cells from mouse embryonic and adult fibroblast cultures by defined factors, Cell 126 (4) (2006) 663–676.
[4] J. Veldhuizen, R.Q. Migrino, M. Nikkhah, Three-dimensional microengineered models of human cardiac diseases, J. Biol. Eng. 13 (2019) 1–12.

[5] P. Beauchamp, C.B. Jackson, L.C. Ozhathil, I. Agarkova, C.L. Galindo, D.B. Sawyer, T.M. Suter, C. Zuppinger, 3D co-culture of hiPSC-derived cardiomyocytes with cardiac fibroblasts improves tissue-like features of cardiac spheroids, Front. Mol. Biosci. 7 (2020) 14.

[6] B. Nugraha, M.F. Buono, L. von Boehmer, S.P. Hoerstrup, M.Y. Emmert, Human cardiac organoids for disease modeling, Clin. Pharmacol. Therapeut. 105 (1) (2019) 79–85.

[7] E. Giacomelli, V. Meraviglia, G. Campostrini, A. Cochrane, X. Cao, R.W. Van Helden, A.K. Garcia, M. Mircea, S. Kostidis, R.P. Davis, Human-iPSC-derived cardiac stromal cells enhance maturation in 3D cardiac microtissues and reveal non-cardiomyocyte contributions to heart disease, Cell Stem Cell 26 (6) (2020) 862–879, e11.

[8] A. Patino-Guerrero, R.D. Ponce Wong, V.D. Kodibagkar, W. Zhu, R.Q. Migrino, O. Graudejus, M. Nikkhah, Development and characterization of isogenic cardiac organoids from human-induced pluripotent stem cells under supplement starvation Regimen, ACS Biomater. Sci. Eng. 9 (2) (2022) 944–958.

[9] A. Patino-Guerrero, J. Veldhuizen, W. Zhu, R.Q. Migrino, M. Nikkhah, Three-dimensional scaffold-free microtissues engineered for cardiac repair, J. Mater. Chem. B 8 (34) (2020) 7571–7590.

[10] D. Zhang, I.Y. Shadrin, J. Lam, H.-Q. Xian, H.R. Snodgrass, N. Bursac, Tissue-engineered cardiac patch for advanced functional maturation of human ESC-derived cardiomyocytes, Biomaterials 34 (23) (2013) 5813–5820.

[11] A. Eder, I. Vollert, A. Hansen, T. Eschenhagen, Human engineered heart tissue as a model system for drug testing, Adv. Drug Deliv. Rev. 96 (2016) 214–224.

[12] Y. Zhao, S. Landau, S. Okhovatian, C. Liu, R.X.Z. Lu, B.F.L. Lai, Q. Wu, J. Kieda, K. Cheung, S. Rajasekar, Integrating organoids and organ-on-a-chip devices, Nat. Rev. Bioeng. (2024) 1–21.

[13] J. Kieda, A. Shakeri, S. Landau, E.Y. Wang, Y. Zhao, B.F. Lai, S. Okhovatian, Y. Wang, R. Jiang, M. Radisic, Advances in cardiac tissue engineering and heart-on-a-chip, J. Biomed. Mater. Res. (2023).

[14] S. Landau, Y. Zhao, H. Hamidzada, G.M. Kent, S. Okhovatian, R.X.Z. Lu, C. Liu, K. T. Wagner, K. Cheung, S.A. Shawky, Primitive macrophages enable long-term vascularization of human heart-on-a-chip platforms, Cell Stem Cell (2024).

[15] A. Mathur, P. Loskill, K. Shao, N. Huebsch, S. Hong, S.G. Marcus, N. Marks, M. Mandegar, B.R. Conklin, L.P. Lee, Human iPSC-based cardiac microphysiological system for drug screening applications, Sci. Rep. 5 (1) (2015) 8883.

[16] K. Ronaldson-Bouchard, D. Teles, K. Yeager, D.N. Tavakol, Y. Zhao, A. Chramiec, S. Tagore, M. Summers, S. Stylianos, M. Tamargo, A multi-organ chip with matured tissue niches linked by vascular flow, Nat. Biomed. Eng. 6 (4) (2022) 351–371.

[17] R.K. Jayne, M.Ç. Karakan, K. Zhang, N. Pierce, C. Michas, D.J. Bishop, C.S. Chen, K. L. Ekinci, A.E. White, Direct laser writing for cardiac tissue engineering: a microfluidic heart on a chip with integrated transducers, Lab Chip 21 (9) (2021) 1724–1737.

[18] J. Veldhuizen, J. Cutts, D.A. Brafman, R.Q. Migrino, M. Nikkhah, Engineering anisotropic human stem cell-derived three-dimensional cardiac tissue on-a-chip, Biomaterials 256 (2020) 120195.

[19] J. Veldhuizen, H.F. Mann, N. Karamanova, W.D. Van Horn, R.Q. Migrino, D. Brafman, M. Nikkhah, Modeling long QT syndrome type 2 on-a-chip via in-depth assessment of isogenic gene-edited 3D cardiac tissues, Sci. Adv. 8 (50) (2022) eabq6720.

[20] J. Veldhuizen, R. Chavan, B. Moghadas, J.G. Park, V.D. Kodibagkar, R.Q. Migrino, M. Nikkhah, Cardiac ischemia on-a-chip to investigate cellular and molecular response of myocardial tissue under hypoxia, Biomaterials 281 (2022) 121336.

[21] J.G. Stinstra, B. Hopenfeld, R.S. MacLeod, On the passive cardiac conductivity, Ann. Biomed. Eng. 33 (2005) 1743–1751.

[22] J. Lee, V. Manoharan, L. Cheung, S. Lee, B.-H. Cha, P. Newman, R. Farzad, S. Mehrotra, K. Zhang, F. Khan, Nanoparticle-based hybrid scaffolds for deciphering the role of multimodal cues in cardiac tissue engineering, ACS Nano 13 (11) (2019) 12525–12539.

[23] S.R. Shin, S.M. Jung, M. Zalabany, K. Kim, P. Zorlutuna, S.b. Kim, M. Nikkhah, M. Khabiry, M. Azize, J. Kong, Carbon-nanotube-embedded hydrogel sheets for engineering cardiac constructs and bioactuators, ACS Nano 7 (3) (2013) 2369–2380.

[24] S.R. Shin, C. Zihlmann, M. Akbari, P. Assawes, L. Cheung, K. Zhang, V. Manoharan, Y.S. Zhang, M. Yüksekkaya, K.t. Wan, Reduced graphene oxide-gelMA hybrid hydrogels as scaffolds for cardiac tissue engineering, Small 12 (27) (2016) 3677–3689.

[25] S.R. Shin, B. Aghaei-Ghareh-Bolagh, X. Gao, M. Nikkhah, S.M. Jung, A. Dolatshahi-Pirouz, S.B. Kim, S.M. Kim, M.R. Dokmeci, X. Tang, Layer-by-layer assembly of 3D tissue constructs with functionalized graphene, Adv. Funct. Mater. 24 (39) (2014) 6136–6144.

[26] M. Kharaziha, S.R. Shin, M. Nikkhah, S.N. Topkaya, N. Masoumi, N. Annabi, M. R. Dokmeci, A. Khademhosseini, Tough and flexible CNT–polymeric hybrid scaffolds for engineering cardiac constructs, Biomaterials 35 (26) (2014) 7346–7354.

[27] S. He, J. Wu, S.-H. Li, L. Wang, Y. Sun, J. Xie, D. Ramnath, R.D. Weisel, T.M. Yau, H.-W. Sung, The conductive function of biopolymer corrects myocardial scar conduction blockage and resynchronizes contraction to prevent heart failure, Biomaterials 258 (2020) 120285.

[28] C.-W. Hsiao, M.-Y. Bai, Y. Chang, M.-F. Chung, T.-Y. Lee, C.-T. Wu, B. Maiti, Z.-X. Liao, R.-K. Li, H.-W. Sung, Electrical coupling of isolated cardiomyocyte clusters grown on aligned conductive nanofibrous meshes for their synchronized beating, Biomaterials 34 (4) (2013) 1063–1072.

[29] A. Navaei, H. Saini, W. Christenson, R.T. Sullivan, R. Ros, M. Nikkhah, Gold nanorod-incorporated gelatin-based conductive hydrogels for engineering cardiac tissue constructs, Acta Biomater. 41 (2016) 133–146.

[30] T. Dvir, B.P. Timko, M.D. Brigham, S.R. Naik, S.S. Karajanagi, O. Levy, H. Jin, K. K. Parker, R. Langer, D.S. Kohane, Nanowired three-dimensional cardiac patches, Nat. Nanotechnol. 6 (11) (2011) 720–725.

[31] A. Navaei, N. Moore, R.T. Sullivan, D. Truong, R.Q. Migrino, M. Nikkhah, Electrically conductive hydrogel-based micro-topographies for the development of organized cardiac tissues, RSC Adv. 7 (6) (2017) 3302–3312.

[32] Y. Li, X. Shi, L. Tian, H. Sun, Y. Wu, X. Li, J. Li, Y. Wei, X. Han, J. Zhang, AuNP-collagen matrix with localized stiffness for cardiac-tissue engineering: enhancing the assembly of intercalated discs by β1-integrin-mediated signaling, Adv. Mater. 28 (46) (2016) 10230–10235.

[33] M. Shevach, S. Fleischer, A. Shapira, T. Dvir, Gold nanoparticle-decellularized matrix hybrids for cardiac tissue engineering, Nano Lett. 14 (10) (2014) 5792–5796.

[34] A. Patino-Guerrero, H. Esmaeili, R.Q. Migrino, M. Nikkhah, Nanoengineering of gold nanoribbon-embedded isogenic stem cell-derived cardiac organoids, RSC Adv. 13 (25) (2023) 16985–17000.

[35] H. Esmaeili, A. Patino-Guerrero, M. Hasany, M.O. Ansari, A. Memic, A. Dolatshahi-Pirouz, M. Nikkhah, Electroconductive biomaterials for cardiac tissue engineering, Acta Biomater. 139 (2022) 118–140.

[36] L. Sun, Z. Chen, D. Xu, Y. Zhao, Electroconductive and anisotropic structural color hydrogels for visual heart-on-a-chip construction, Adv. Sci. 9 (16) (2022) 2105777.

[37] K. Roshanbinfar, M. Kolesnik-Gray, M. Angeloni, S. Schruefer, M. Fiedler, D. W. Schubert, F. Ferrazzi, V. Krstic, F.B. Engel, Collagen hydrogel containing polyethylenimine-gold nanoparticles for drug release and enhanced beating properties of engineered cardiac tissues, Adv. Healthcare Mater. (2023) 2202408.

[38] H. Li, B. Yu, P. Yang, J. Zhan, X. Fan, P. Chen, X. Liao, C. Ou, Y. Cai, M. Chen, Injectable AuNP-HA matrix with localized stiffness enhances the formation of gap junction in engrafted human induced pluripotent stem cell-derived cardiomyocytes and promotes cardiac repair, Biomaterials 279 (2021) 121231.

[39] H. Esmaeili, A. Patino-Guerrero, R.A. Nelson Jr., N. Karamanova, T.M. Fisher, W. Zhu, F. Perreault, R.Q. Migrino, M. Nikkhah, Engineered gold and silica nanoparticle-incorporated hydrogel scaffolds for human stem cell-derived cardiac tissue engineering, ACS Biomater. Sci. Eng. (2024).

[40] C.M. Cobley, J. Chen, E.C. Cho, L.V. Wang, Y. Xia, Gold nanostructures: a class of multifunctional materials for biomedical applications, Chem. Soc. Rev. 40 (1) (2011) 44–56.

[41] L. Karperien, A. Navaei, B. Godau, A. Dolatshahi-Pirouz, M. Akbari, M. Nikkhah, Nanoengineered biomaterials for cardiac regeneration, Nanoengineered Biomaterials for Regenerative Medicine, Elsevier2019, pp. 95-124.

[42] J. Veldhuizen, M. Nikkhah, Developing 3D organized human cardiac tissue within a microfluidic platform, JoVE J. (172) (2021) e62539.

[43] X. Lian, J. Zhang, S.M. Azarin, K. Zhu, L.B. Hazeltine, X. Bao, C. Hsiao, T.J. Kamp, S.P. Palecek, Directed cardiomyocyte differentiation from human pluripotent stem cells by modulating Wnt/β-catenin signaling under fully defined conditions, Nat. Protoc. 8 (1) (2013) 162–175.

[44] S. Tohyama, F. Hattori, M. Sano, T. Hishiki, Y. Nagahata, T. Matsuura, H. Hashimoto, T. Suzuki, H. Yamashita, Y. Satoh, Distinct metabolic flow enables large-scale purification of mouse and human pluripotent stem cell-derived cardiomyocytes, Cell Stem Cell 12 (1) (2013) 127–137.

[45] J. Zhang, R. Tao, K.F. Campbell, J.L. Carvalho, E.C. Ruiz, G.C. Kim, E.G. Schmuck, A.N. Raval, A.M. da Rocha, T.J. Herron, Functional cardiac fibroblasts derived from human pluripotent stem cells via second heart field progenitors, Nat. Commun. 10 (1) (2019) 2238.

[46] J. Schindelin, I. Arganda-Carreras, E. Frise, V. Kaynig, M. Longair, T. Pietzsch, S. Preibisch, C. Rueden, S. Saalfeld, B. Schmid, Fiji: an open-source platform for biological-image analysis, Nat. Methods 9 (7) (2012) 676–682.

[47] L. Sala, B.J. Van Meer, L.G. Tertoolen, J. Bakkers, M. Bellin, R.P. Davis, C. Denning, M.A. Dieben, T. Eschenhagen, E. Giacomelli, MUSCLEMOTION: a versatile open software tool to quantify cardiomyocyte and cardiac muscle contraction in vitro and in vivo, Circ. Res. 122 (3) (2018) e5–e16.

[48] N. Brookhouser, S. Raman, C. Frisch, G. Srinivasan, D.A. Brafman, APOE2 mitigates disease-related phenotypes in an isogenic hiPSC-based model of Alzheimer's disease, Mol. Psychiatr. 26 (10) (2021) 5715–5732.

[49] B. Nikoobakht, M.A. El-Sayed, Preparation and growth mechanism of gold nanorods (NRs) using seed-mediated growth method, Chem. Mater. 15 (10) (2003) 1957–1962.

[50] Y. Li, X. Shi, L. Tian, H. Sun, Y. Wu, X. Li, J. Li, Y. Wei, X. Han, J. Zhang, AuNP–collagen matrix with localized stiffness for cardiac-tissue engineering: enhancing the assembly of intercalated discs by β1-integrin-mediated signaling, Adv. Mater. 28 (46) (2016) 10230–10235.

[51] K. Zhu, S.R. Shin, T. van Kempen, Y.C. Li, V. Ponraj, A. Nasajpour, S. Mandla, N. Hu, X. Liu, J. Leijten, Gold nanocomposite bioink for printing 3D cardiac constructs, Adv. Funct. Mater. 27 (12) (2017) 1605352.

[52] A.J. Engler, C. Carag-Krieger, C.P. Johnson, M. Raab, H.-Y. Tang, D.W. Speicher, J. W. Sanger, J.M. Sanger, D.E. Discher, Embryonic cardiomyocytes beat best on a matrix with heart-like elasticity: scar-like rigidity inhibits beating, J. Cell Sci. 121 (22) (2008) 3794–3802.

[53] X. Yang, L. Pabon, C.E. Murry, Engineering adolescence: maturation of human pluripotent stem cell–derived cardiomyocytes, Circ. Res. 114 (3) (2014) 511–523.

[54] J.H. Tsui, A. Leonard, N.D. Camp, J.T. Long, Z.Y. Nawas, R. Chavanachat, A. S. Smith, J.S. Choi, Z. Dong, E.H. Ahn, Tunable electroconductive decellularized extracellular matrix hydrogels for engineering human cardiac microphysiological systems, Biomaterials 272 (2021) 120764.

[55] C. Fan, Y. Tang, M. Zhao, X. Lou, D. Pretorius, P. Menasche, W. Zhu, J. Zhang, CHIR99021 and fibroblast growth factor 1 enhance the regenerative potency of human cardiac muscle patch after myocardial infarction in mice, J. Mol. Cell. Cardiol. 141 (2020) 1–10.
[56] X.Q. Xu, S.Y. Soo, W. Sun, R. Zweigerdt, Global expression profile of highly enriched cardiomyocytes derived from human embryonic stem cells, Stem Cell. 27 (9) (2009) 2163–2174.
[57] D.A. Pijnappels, M.J. Schalij, J. van Tuyn, D.L. Ypey, A.A. de Vries, E.E. van der Wall, A. van der Laarse, D.E. Atsma, Progressive increase in conduction velocity across human mesenchymal stem cells is mediated by enhanced electrical coupling, Cardiovasc. Res. 72 (2) (2006) 282–291.
[58] J.M. Churko, P. Garg, B. Treutlein, M. Venkatasubramanian, H. Wu, J. Lee, Q. N. Wessells, S.-Y. Chen, W.-Y. Chen, K. Chetal, Defining human cardiac transcription factor hierarchies using integrated single-cell heterogeneity analysis, Nat. Commun. 9 (1) (2018) 4906.
[59] T. Grancharova, K.A. Gerbin, A.B. Rosenberg, C.M. Roco, J.E. Arakaki, C. M. DeLizo, S.Q. Dinh, R.M. Donovan-Maiye, M. Hirano, A.M. Nelson, J. Tang, J. A. Theriot, C. Yan, V. Menon, S.P. Palecek, G. Seelig, R.N. Gunawardane, A comprehensive analysis of gene expression changes in a high replicate and open-source dataset of differentiating hiPSC-derived cardiomyocytes, Sci. Rep. 11 (1) (2021) 15845.
[60] P. Bouvagnet, S. Neveu, M. Montoya, J. Leger, Development changes in the human cardiac isomyosin distribution: an immunohistochemical study using monoclonal antibodies, Circ. Res. 61 (3) (1987) 329–336.
[61] L. Gorza, J. Mercadier, K. Schwartz, L. Thornell, S. Sartore, S. Schiaffino, Myosin types in the human heart. An immunofluorescence study of normal and hypertrophied atrial and ventricular myocardium, Circ. Res. 54 (6) (1984) 694–702.
[62] C. Xu, Differentiation and enrichment of cardiomyocytes from human pluripotent stem cells, J. Mol. Cell. Cardiol. 52 (6) (2012) 1203–1212.
[63] C.E. Friedman, Q. Nguyen, S.W. Lukowski, A. Helfer, H.S. Chiu, J. Miklas, S. Levy, S. Suo, J.-D.J. Han, P. Osteil, Single-cell transcriptomic analysis of cardiac differentiation from human PSCs reveals HOPX-dependent cardiomyocyte maturation, Cell Stem Cell 23 (4) (2018) 586–598, e8.
[64] Fikru B. Bedada, Sunny S.-K. Chan, Stefania K. Metzger, L. Zhang, J. Zhang, Daniel J. Garry, Timothy J. Kamp, M. Kyba, Joseph M. Metzger, Acquisition of a quantitative, stoichiometrically conserved ratiometric marker of maturation status in stem cell-derived cardiac myocytes, Stem Cell Rep. 3 (4) (2014) 594–605.
[65] K. Ronaldson-Bouchard, S.P. Ma, K. Yeager, T. Chen, L. Song, D. Sirabella, K. Morikawa, D. Teles, M. Yazawa, G. Vunjak-Novakovic, Advanced maturation of human cardiac tissue grown from pluripotent stem cells, Nature 556 (7700) (2018) 239–243.
[66] S. Gill, J. Veinot, M. Kavanagh, O. Pulido, Human heart glutamate receptors—implications for toxicology, food safety, and drug discovery, Toxicol. Pathol. 35 (3) (2007) 411–417.
[67] S. Reilly, S. Nattel, Finding a new job: glutamate signaling acts in atrial cardiomyocytes, Cell Res. 31 (9) (2021) 943–944.
[68] X.-D. Zhang, P.N. Thai, L. Ren, M.C.P. Flores, H.A. Ledford, S. Park, J.H. Lee, C.-R. Sihn, C.-W. Chang, W.C. Chen, Prestin amplifies cardiac motor functions, Cell Rep. 35 (5) (2021).
[69] T. Grancharova, K.A. Gerbin, A.B. Rosenberg, C.M. Roco, J.E. Arakaki, C. M. DeLizo, S.Q. Dinh, R.M. Donovan-Maiye, M. Hirano, A.M. Nelson, A comprehensive analysis of gene expression changes in a high replicate and open-source dataset of differentiating hiPSC-derived cardiomyocytes, Sci. Rep. 11 (1) (2021) 15845.
[70] B.E. Bernstein, J.A. Stamatoyannopoulos, J.F. Costello, B. Ren, A. Milosavljevic, A. Meissner, M. Kellis, M.A. Marra, A.L. Beaudet, J.R. Ecker, The NIH roadmap epigenomics mapping consortium, Nat. Biotechnol. 28 (10) (2010) 1045–1048.
[71] M.N. Hirt, A. Hansen, T. Eschenhagen, Cardiac tissue engineering: state of the art, Circ. Res. 114 (2) (2014) 354–367.
[72] Y. Tang, F. Tian, X. Miao, D. Wu, Y. Wang, H. Wang, K. You, Q. Li, S. Zhao, W. Wang, Heart-on-a-chip using human iPSC-derived cardiomyocytes with an integrated vascular endothelial layer based on a culture patch as a potential platform for drug evaluation, Biofabrication 15 (1) (2022) 015010.
[73] N. Huebsch, B. Charrez, G. Neiman, B. Siemons, S.C. Boggess, S. Wall, V. Charwat, K.H. Jæger, D. Cleres, Å. Telle, Metabolically driven maturation of human-induced-pluripotent-stem-cell-derived cardiac microtissues on microfluidic chips, Nat. Biomed. Eng. 6 (4) (2022) 372–388.
[74] Y. Wu, L. Wang, B. Guo, P.X. Ma, Interwoven aligned conductive nanofiber yarn/hydrogel composite scaffolds for engineered 3D cardiac anisotropy, ACS Nano 11 (6) (2017) 5646–5659.
[75] M. Morsink, P. Severino, E. Luna-Ceron, M.A. Hussain, N. Sobahi, S.R. Shin, Effects of electrically conductive nano-biomaterials on regulating cardiomyocyte behavior for cardiac repair and regeneration, Acta Biomater. 139 (2022) 141–156.
[76] J.-O. You, M. Rafat, G.J. Ye, D.T. Auguste, Nanoengineering the heart: conductive scaffolds enhance connexin 43 expression, Nano Lett. 11 (9) (2011) 3643–3648.
[77] Y.-d. Yu, Y.-t. Xue, Y. Li, Identification and verification of feature biomarkers associated in heart failure by bioinformatics analysis, Sci. Rep. 13 (1) (2023) 3488.
[78] S. McLennan, X. Wang, V. Moreno, D. Yue, S. Twigg, Connective tissue growth factor mediates high glucose effects on matrix degradation through tissue inhibitor of matrix metalloproteinase type 1: implications for diabetic nephropathy, Endocrinology 145 (12) (2004) 5646–5655.
[79] M.S. Ahmed, J. Gravning, V.N. Martinov, T.G. von Lueder, T. Edvardsen, G. Czibik, I.T. Moe, L.E. Vinge, E. Øie, G. Valen, Mechanisms of novel cardioprotective functions of CCN2/CTGF in myocardial ischemia-reperfusion injury, Am. J. Physiol. Heart Circ. Physiol. 300 (4) (2011) H1291–H1302.
[80] F. Buffolo, M. Tetti, P. Mulatero, S. Monticone, Aldosterone as a mediator of cardiovascular damage, Hypertension 79 (9) (2022) 1899–1911.
[81] M. Fukuchi, M. Nakajima, Y. Fukai, T. Miyazaki, N. Masuda, M. Sohda, R. Manda, K. Tsukada, H. Kato, H. Kuwano, Increased expression of c-Ski as a co-repressor in transforming growth factor-β signaling correlates with progression of esophageal squamous cell carcinoma, Int. J. Cancer 108 (6) (2004) 818–824.
[82] Y. Cai, F. Ying, H. Liu, L. Ge, E. Song, L. Wang, D. Zhang, E. Hoi Ching Tang, Z. Xia, M.G. Irwin, Deletion of Rap1 protects against myocardial ischemia/reperfusion injury through suppressing cell apoptosis via activation of STAT3 signaling, FASEB J. 34 (3) (2020) 4482–4496.